Title of thesis: NORMAL AND BARRETT'S ESOPHAGUS PHANTOM FOR OPTICAL COHERENCE TOMOGRAPHY (OCT) SYSTEMS EVALUATED USING TEXTURE ANALYSIS METHODS

Abbas Bandukwala, Master of Science, 2017

Thesis directed by: Professor Sheryl Ehrman
Department of Chemical Engineering

Abstract: Optical coherence tomography (OCT) is increasingly used to image tissue microstructure for diagnostic purposes. OCT imaging is currently being researched to diagnose, survey, and monitor Barrett's esophagus. However due to the many differences between OCT systems, a method to calibrate or provide a standard is needed.

This research developed esophagus phantoms that represent normal and Barrett's esophagus tissue. When imaged by OCT systems the phantoms mimicked the visual aspects of the normal esophagus tissue and Barrett's esophagus tissue. The images produced with the phantom were then evaluated with three different texture analysis methods to quantify the phantoms. Finally, the images from the phantoms were compared to clinical images for visual alignment and texture accuracy. The results demonstrated that these esophagus phantoms can be distinguished both visually and through quantifying the images in the texture.

NORMAL AND BARRETT'S ESOPHAGUS PHANTOM FOR OPTICAL COHERENCE TOMOGRAPHY (OCT) SYSTEMS EVALUATED USING TEXTURE ANALYSIS METHODS

By

Abbas Q. Bandukwala

Thesis submitted to the Faculty of the Graduate School of the
University of Maryland, College Park, in partial fulfillment
of the requirements for the degree of
Master of Science
2017

Advisory Committee:

Professor Sheryl Ehrman, Chair
Professor Yu Chen
Professor Nam Sum Wang
Professor Taylor Woehl
Dr. Joshua Pfefer

Table of Contents

List of Figures and Tables

1.1 Overview - Normal esophagus and Barrett's Esophagus (BE)

The esophagus is a muscular tube like organ that connects the pharynx to the stomach. It is around 25cm long and 2cm in diameter in an adult. The esophagus is comprised of 5 different tissue layers. The surface layer of the esophagus is known as the mucosal epithelium which is about 350-450um in thickness [1, 6]. The following layer of tissue, the laminar propria, is a connective tissue layer about 200-300um thick. Below the laminar propria, the esophagus is composed of the musclaris mucosae (~300um), submucosa (~200um), and musularis propria[1]. Each of these layers is distinct and the thickness of the first three layers can vary from the upper esophagus to the lower esophagus (Figure 3). Changes in the mucosa and layer structure of the esophagus are a concern because this could be a precursor to a disease state.

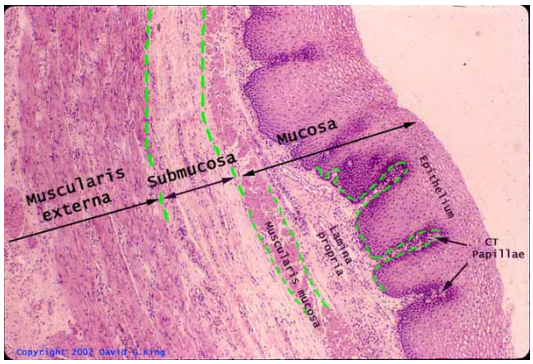

Figure 1 Histology of normal esophagus. Image from http://www.siumed.edu/~dking2/erg/GI005b.jpg, copyright David G. King, used with permission

One type of change that can occur in the epithelium and below the surface of the epithelium is specialized intestinal metaplasia also known as Barrett's Esophagus (BE) (Figure 4). Barrett's Esophagus is developed from Gastroesophageal Reflux Disease (GERD). In this condition, contents from the stomach are forced back through the esophagastric junction. Exposing the

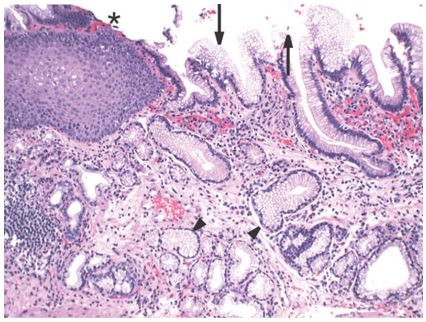

Figure 2 Histology of Barrett Esophagus[2].

esophagus to these gastric contents over a long period of time can cause changes in the squamous mucosa and lead to the development of BE. A widely accepted definition, which was published in2008 by the American College of Gastroenterology (ACG) defined Barrett's Esophagus as "a change in the distal esophageal epithelium of any length that can be recognized as columnar type mucosa at endoscopy and is confirmed to have intestinal metaplasia by biopsy of the tubular esophagus."[7, 8] Barrett's esophagus can be a precursor to dysplasia and these patients are predisposed to develop esophageal adenocarcinoma. Esophageal adenocarcinoma diagnosis rates have increased significantly and continue to increase[7, 8]. Because BE is considered a risk factor for adenocarcinoma, the patient requires routine monitoring and surveillance after diagnosis. Monitoring BE, physicians can identify further changes in the BE and treat patients before the onset of adenocarcinoma. BE is not associated with squamous cell carcinoma.

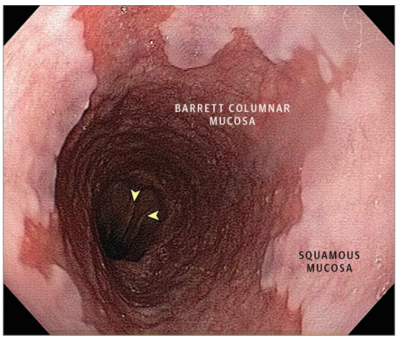

Figure 3 Normal and BE areas seen during an endoscopy. The white upper portion is the normal esophagus portion and the lower pink portion is BE.[5]

When viewed from an endoscope, BE has a rough and brownish appearance and the squamous epithelium can appear thicker[1]. Normal esophagus tissue will have a white / pink - grey appearance but changes to a red-pink near the esophagogastric junction[9]. Histologically, many changes of BE tissue are identifiable. Many changes that occur to the epithelial layer are slightly below the surface and these changes cannot be seen during a white light endoscopic procedure, which is currently the primary method used to visualize and examine the

esophagus. BE tissue can be identified by a thicker epithelial layer and disruption of the 5 layers that are associated with normal esophageal tissue. Goblet cells and gland structures are also found throughout the BE tissue sample. Short segment BE is defined as BE that is less than 3cm in length while long segment BE is any BE greater than 3cm [10].

The ACG recommends a person who is diagnosed with BE receive an endoscopic procedure to monitor the BE area. A percentage of people who have BE develop dysplasia, and approximately 0.5% of patients with long segment BE go on to develop adenocarcinoma every year[10] [8]. The 2015 ACG guidelines found that 3 in 1000 person with BE will develop adenocarcinoma every year[7]. Adenocarcinoma is significantly higher in subject who have BE with high-grade dysplasia. About 6% or these patients develop adenocarcinoma every year[7]. Short segment BE is not considered a significant concern for developing adenocarcinoma[10]. Even though a patient with BE has a small chance of developing adenocarcinoma, the patient must be monitored because of the limited treatment options and high mortality from this cancer.

1.2 Overview - Current Medical Methods to Diagnose and Survey BE

As stated above, the current standard of medicine evaluates and monitors BE using white light endoscopy and biopsy procedures which only provides a surface view of the esophagus tissue. For patients who are at risk of developing BE, the physician will employ a biopsy method called the "Seattle protocol"[7]. During the endoscopy procedure four biopsy samples are taken from each quadrant every 2cm for the full length of the esophagus. If any surface irregularities are seen from the

endoscope during the procedure, the physician would also take biopsies from that abnormal area of the esophagus[7]. Biopsies are needed to confirm changes in the mucosa and the development of intestinal metaplasia. Changes such as glandular structures and goblet cells are not visible during the endoscopic procedure, but biopsies samples can confirm these changes in the tissue. These biopsies must be analyzed by a pathologists to confirm the presence of BE [10]. The Seattle protocol screening method may not be effective because this method samples a fraction of the esophagus. There is a risk that an areas with BE could be missed by using this protocol. In 2015, the ACG guidelines reported that there was a 35% percent increase in finding BE with intestinal metaplasia if 4 biopsies were taken and up to 68% yield if 8 biopsies were obtained [10].

Patients who do have BE need surveillance endoscopies and biopsies every 3-5 years to determine if dysplastic changes in the BE tissue are occurring[10]. If dysplasia does develop in these BE areas, the patient requires endoscopic surveillance and biopsies more frequently. The medical literature indicates that patients have a better chance of survival when dysplasia and adenocarcinoma are detected early[7, 10]. Therapeutic procedures can treat areas of high grade dysplasia and prevent the development of adenocarcinoma[11]. If proper diagnosis and surveillance of BE does not occur early, then patients are at risk of developing cancer which effects their survival chance. Because white light endoscopic procedures do not provide visualization beneath the surface of the epithelial layer, physicians are unable to determine if BE is present, or if they are moving over a suspected BE area that needs to be biopsied. Even though BE does affect the

epithelial layer, this condition is not always visible on the surface of this layer. Physicians need a method to visualize the tissue below the surface of the tissue. Having information below the surface would allow the physician to take target biopsies. It would also improve assessing the full esophagus tissue as oppose to a fraction of the tissue using the current Seattle protocol method.

In 2008, the American College of Gastroenterology anticipated that optical imaging techniques will become clinically available[7]. Some medical devices can provide some limited information of the tissue below the surface during the endoscopic procedure. For example Narrow Band Imaging (NBI), uses a filter to allow certain wavelengths of light to be received from the tissue into the viewing area. Because certain wavelengths of light are able to penetrate deeper into the tissue, and are absorbed and reflected by the different tissue layers, oxygenated and deoxygenated blood, and other tissue structure, the physician can gather additional information below the tissue surface. The vascularization or blood flow may be visible using NBI, but this method does not provide an image of the tissue below the surface. Therefore, a physician cannot assess and determine if BE lies beneath the surface using this method. The current standard of medicine has limitations that could prevent the proper evaluation of the esophagus tissue. Optical Coherence Tomography (OCT) imaging could alleviate these current white light visualization limitations by providing images of esophagus tissue, which include images beneath the surface. OCT imaging has the potential to greatly improve the location, evaluation, and surveillance of BE in clinical use. Some researchers are developing algorithms that can help identify areas of interest based on analyzing the image and

specifically the image texture[12]. Based on previous and current research in this area, OCT imaging has great potential in improving the current standard of care by imaging the esophageal tissue microstructure.

1.3 Overview - Basic Principles of OCT

Optical coherence tomography (OCT) is an imaging modality that can provide two and three dimensional micrometer scale images in real time. This imaging technology is being heavily researched for many different medical purposes. Because OCT can provide images with a resolution of 5-20 μ m and image the tissue 1-2mm beneath the surface, this imaging method can help physicians visualize details of the tissue microstructure and cellular structure. The tissue can be imaged *in situ* and does not need to be removed to create the image.

OCT is a light based imaging technology that uses infrared light, which is backscattered from the tissue to create an image. OCT is similar to ultrasound in that both methods measure the echo time delay and the return intensity of the signal to produce an image[13]. Because the wavelength of light is significantly shorter than sound, OCT can produce higher resolution images than ultrasound methods. To measure the time delay of the signal, a device, known as Michelson interferometer, is used to collect and measure a reference signal and the return signal from the

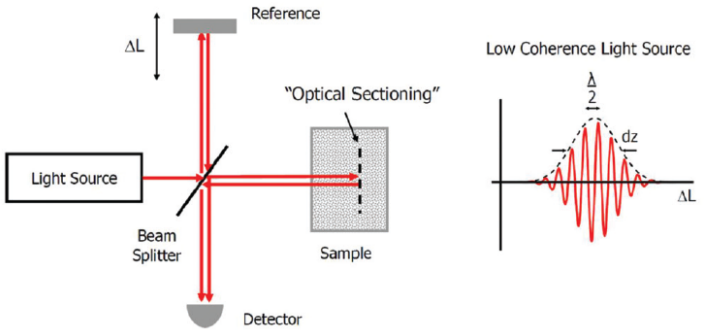

Figure 4 Schematic of Michelson Interferometer and Low Coherence Light source.[3] ΔL = path length of reference arm, dz = axial resolution,

tissue. Low coherence interferometry is the interference of light beams which are limited by the coherence length of the light source[13]. A low coherent light source could be superluminescent diodes or femtosecond pulsed lasers such as Ti:Sapphire or Cr:Forsterite lasers[3]. These low coherent light sources emit light with a broad bandwidth. In the diagram shown in Figure 4, light from the light source is split between the sample arm and the reference arm. The light scattered back from the sample and the reference arm is then evaluated. Interference between the reference signal and the sample signal occur when the delay between the two signals is within the coherence length of the light source[13]. Only single scattered light or very little scatter light maintains the coherence that is then analyzed by the interferometer. By measuring the time delay of the sample and the intensity of the return light of the sample signal, low coherence interferometry can measure the depth of the sample and create imaging information. A single signal provides one-dimensional information of the sample and this one return signal is known as an A-scan. An OCT system scans an area using the low coherence interferometry method to collect multiple A-scans to produce a two- dimensional cross-sectional image or tomography of the sample also known as a B-scan.

The first OCT systems developed were time domain (TD) OCT systems. In this system, the reference arm was a mirror that would move. This mirror movement would reject the sample signal that had a different optical path length of the mirror. This method enables imaging of 1-10 frames per second[13]. The next OCT systems developed uses Fourier transform to analyze the return signal. There are two types of Fourier domain (FD) OCT systems, spectral/Fourier

domain OCT and swept-source (SS)-OCT or Optical frequency domain imaging (OFDI)[13].

Spectral/Fourier OCT uses a high-speed line scan camera and a spectrometer to measure the interference pattern for many signals at one time. SS-OCT uses a frequency swept laser source and photodetector to evaluate many interference signals at different depths. Because FD-OCT can evaluate many interference signals at one time, it is approximately 100 times faster than TD-OCT. SS-OCT can also be used with longer wavelength lasers (1000-1300nm). These longer wavelengths can penetrate deeper into tissue enabling images at greater depths than the shorter wavelengths (800-900nm) used in OCT systems. SS-OCT systems can be used in highly scattering tissue, which makes these systems able to image different types of tissue including diseases tissue [13].

As stated above, OCT can create images with resolution similar to a light microscope. Axial resolution and lateral resolution are determined independently each other. The light source coherence length defines the axial resolution of the system. The lateral resolution of the OCT system is dependent on the optics of the imaging device. To increase the transverse resolution, a small spot size can be used and the lens should have a high numerical aperture[13]. Increasing the lateral resolution decreases the depth range of the system.

Many different types of probes are available for use with OCT systems. The clinical application of the OCT system dictates the design of method used to transmit and receive the light signal from the sample. Fiber optic cable can be used in endoscopes and

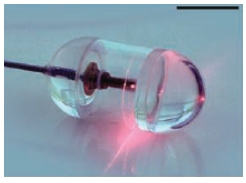

Figure 5 OCT probe used to image the esophagus[4].

other types of probes that are needed to image internal organs and structures such as the esophagus and the GI system, and arteries and veins. Hand held probes can be used to image the skin and ex vivo tissue samples. Most OCT systems are comprised of a monitor, computer base, and probe which are attached by a wire. The systems can be transported to different rooms on a cart.

OCT systems operate using the same principles described above, but many variations can exist from system to system. The software to process the signal is not identical in each system. The facility can write custom code to have the signal processed and analyzed as needed. Because the software on each system can analyze the signal in a different manner, the image produced can also vary. Other factors can also affect the signal and the final image. As stated above different probes are being developed for the same clinical application. These probes can have different optics which again changes the way the signal is sent out of the probe and then received from the sample. Finally, there is a significant difference between types of tissue. The eye and skin tissue would have different optical and scattering properties then tissue in the bladder or esophagus[13]. One standard may not be able to assess OCT systems for the different medical specialties. For these reasons, specific tissue type standards are needed to assess the imaging capabilities between different OCT systems used for the same clinical purpose. A standard system or method would allow a level of quality to be determined. A standard system can represent a universally accepted method to determine performance and measure specific parameters.

Today, more and more clinical imaging applications are being explored using

OCT systems. Ophthalmology was the first area where OCT imaging was accepted and made significant contributions for imaging different areas of the eye[13]. Another medical area under heavy research using OCT imaging is gastroenterology. OCT probes can easily access the tubular organs in the gastrointestinal tract by means of endoscopic procedures. OCT systems and probes are being developed to provide information below the surface of these organs where abnormal changes to the cellular structure can occur. OCT has the potential to improve surveillance and diagnostic capabilities in gastroenterology clinical applications.

1.4 Overview - Tissue Phantoms

Currently, optical imaging systems are assessed, calibrated, and evaluated with basic phantom that do not mimic a specific tissue structure. Tissue phantoms or biomimetric phantoms mimic the properties of real tissue structure. Phantoms can assess a system's imaging ability to function within its given parameters. Phantoms assess imaging parameters such as resolution, depth of penetration, frame rate, signal to noise ratio, and image distortion and other imaging parameters. Another purpose of phantoms is to compare the function between two different systems. Depending on the imaging systems and the intended use, biomimetric phantom should incorporate the traits of the tissue it represents. Phantoms should have the optical properties and have the visual characteristics of the specific tissue. Because OCT collects data from back scattered light from the tissue, the correct scattering coefficient is an important property for the phantom. Other properties such as the index of refraction and absorption coefficient should also be considered when constructing the biomimetric phantom. In addition to having the optical

properties of the tissue, the phantom should also produce an image similar to the tissue. Layers and any other significant tissue structures that could appear in the image should also be designed into the phantom. Using the different tissue properties, one can design phantoms that represent specific types of normal or diseased tissue. For example, phantoms can be constructed to mimic normal or diseased esophageal tissue.

Because there is variability in the tissue of the organ between person to person and there can even be variability in the tissue at different areas of the organ, it is challenging to validate a system's abilities and images with *in vivo* or *ex vivo* tissue. Validated scales and measurements are necessary, because scales that are not validated are using unknown measurements that are not verified. Precise and accurate scales which are validated are needed when assessing a system. Phantoms function as a standard that assess the performance of one system or many different systems. In addition, quantitative functions can be derived for use with phantoms to assess system metrics such as axial and lateral resolution. Quantitative functions can also be derived to determine similarities or differences for specific types of tissue.

Many tissue phantoms constructed for use with OCT systems are made with a silicone based material such as polydimethylsiloxane (PDMS)[14] . PDMS has a refractive index of 1.41[15]. PDMS is the base material for the tissue phantom. It is a viscous liquid, and when mixed with a cross linking curing agent becomes a solid object. PDMS is ideal to use because it can be molded or shaped into large, small, or thin structures. There are different types of PDMS that are sold by companies such

as DOW/Corning.

PDMS by itself is a transparent material. To create the scattering properties and visual structure of tissue, scattering particles are mixed into the PDMS in varying concentration. Most phantoms are constructed with titanium dioxide (TiO_2), barium sulfate ($BaSO_4$), or silicon dioxide (SiO_2) scattering particles. The individual size of these particles is small enough to not be seen as a structure in the image. These particles are also compatible with PDMS. PDMS is a hydrophobic material and cannot be mixed with particles that contain water[15]. Organic material also cannot be mixed with PDMS. In *in vivo* tissue, the layers in a tissue have different cell types, which is the reason for the change in visual appearance of these layers in the image. Different particles can be used in the separate layers of the phantom to create layers with the desired scattering coefficient and visual image. One can also vary the concentration of the scattering particle for each separate layer to have visibly different layers and scattering coefficients. Even though the scattering particles do not have the same index of refraction as the PDMS, the particles do not significantly alter the index of refraction of the PDMS when mixed together. Because of the index of refraction mismatch, these particles scatter the light when mixed with PDMS. The scattering particles create the tissue layers and background. The scattering particles do not represent cells or a specific structure in the tissue.

Other matrix material such as gelatin can be mixed with other types of scattering particles to create a phantom that can be used with OCT. Gelatin phantoms can be mixed with scattering particles such as silica beads or organic

compounds, but a major disadvantage of gelation phantoms is durability. These gelatin phantoms degrade quickly because these phantoms can begin to evaporate within hours of being constructed, and the repeated use is limited. PDMS phantoms on the other hand will maintain the structural and physical properties for a many months. OCT phantoms have been constructed from other material but it appears for OCT systems, most tissue mimicking phantoms are made from PDMS.

Phantoms that represent an eye[16] and bladder[17] have been constructed. Both of these groups constructed the phantoms with PDMS and the scattering particles listed above. These phantoms successfully mimicked the tissue layers that compose these organs. Both of these phantoms show the importance of developing phantoms that represent a specific tissue type. OCT can image both of these organs even though the structure and appearance of these organs are significantly different. The retina phantom mimics the many very thin layers that compose this organ. The bladder phantom is a much bigger organ with 3 distinct tissue layers. In addition, two distinct OCT systems would image these organs. Because the retina is significantly thinner than the walls of the bladder, 850nm wavelength OCT systems can produce the necessary detail and image of this organ. While a 1350nm wavelength system is needed to image the bladder and penetrate deeper into the bladder tissue. The probes used to image these organs would have different shapes, and structure. For these reasons, two distinct phantoms that represent these organs are needed to analyze the performance of the

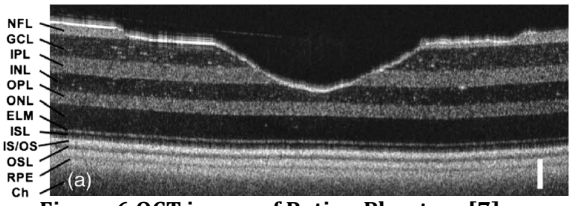

Figure 6 OCT image of Retina Phantom [7].

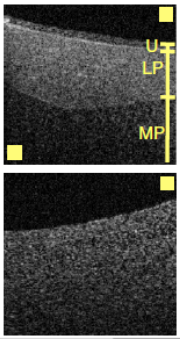

Figure 7 OCT image of Bladder phantom [8].

OCT systems imaging these organs.

Recently, more researchers are developing algorithms to differentiate tissue types, which include diseased tissue such as precancerous tissue and cancerous tissue. Some of these algorithms assess these different tissue types based on change in image texture. Phantoms can determine the effectiveness of these algorithms during the research phase of development of the device, and calibration of the system. These systems could be designed to analyze the full esophagus and assisted with taking targeted biopsies.

Phantoms could help facilitate OCT imaging into clinical practice. Phantoms can play a role in the development of imaging systems, performance assessment of imaging systems, and finally calibration of a system in clinical use. Most of the current phantoms used to assess OCT systems do not represent the intended tissue, and therefore do not provide a method to test the system when used in these different tissue types. By measuring the system performance with phantoms that represent the tissue, researchers and manufacturers can develop systems, software and probes that are optimized to image the desired tissue accurately. Other imaging modalities such as MRI systems and CT systems also have phantoms to test the system. These systems, though, do not require tissue specific phantoms.

1.5 Overview - Outline of the Thesis

OCT imaging could provide the needed visual information beneath the tissue surface to make a better diagnosis of the tissue. Infrared light can penetrate the esophagus tissue up to 2mm. OCT images can provide micron scale images of the mucosa, which would include the cellular structure of the esophagus. As stated

above, OCT imaging is advancing from the research phase into clinical applications for many medical fields and especially into gastroenterology. Phantoms of the esophagus could help facilitate this technology into more esophageal clinical procedures.

The goal of this thesis is to create phantoms that represent the visual and optical properties of both normal and Barrett's Esophagus for use with OCT imaging systems and evaluating these phantoms with three different image texture analysis methods. These phantoms will be compared to each other and clinical images to assess how accurately the phantoms represent the visual aspects of these types of tissues. A quantitative comparison should also demonstrate the differences between the two types of phantoms. Statistical methods described in section 2 will be applied to analyze the image texture through changes in pixel intensity and speckle characteristics between the two phantoms. A comparison of the normal esophagus phantom and normal esophagus clinical images, and BE phantom and BE clinical images will also be conducted using the same quantitative methods.

Section 3 of this thesis will present the detailed procedure to create the phantom. The material to construct the phantom will be described and the method to create the correct image texture necessary to mimic the tissue will also be discussed. This section will also provide the details of the imaging systems operated in the study and the system settings to image the phantoms. It is also important to outline the technique to image the phantoms. If the imaging technique changes between users or from system to system, the phantoms should still be able to provide feedback of how the system is functioning. This section will conclude with a

discussion on the deficiencies in the construction of the phantom, OCT system shortcomings, and imaging techniques. Based on these problems encountered in construction and imaging of the phantom, suggested improvements for future research will be recommended.

The next section will explain the results and analyze the clinical and phantom images. This section will first describe both the visual and quantitative characteristics of the esophageal clinical images taken by an OCT system under research at another institution. Next, images of the phantoms and assessment of the phantoms will be provided. After providing the phantom information, a visual and quantitative comparison of the clinical and phantom images will be presented. Finally, the last portion of this section will discuss the results and detail any observations or problems encountered during the analysis and comparison of the clinical and phantom images.

Finally, the conclusion section of the thesis will summarize the purpose of this thesis study and the results obtained during this study. The conclusion section will discuss any limitations of this study and the phantom. Lastly the thesis will propose thoughts on any future considerations for follow on research to create phantoms representing specific tissue types for use with OCT systems.

2.1 Texture Analysis Methods - Introduction

Image texture can be defined as the spatial distribution of pixel intensities in an image[18]. These distribution of pixel intensities, or image texture, can be analyzed and quantified to classify, segment or detect information in an image[18]. In an image where the pixel intensities vary greatly from pixel to pixel, the image can be described as having rough image texture or heterogeneous texture. If the pixel intensities values are similar or do not have much variations between pixels, then the image texture is considered to be smooth or homogenous. Rough and smooth image textures are not defined, and are subjective based on the images being compared. Image texture and pixel intensity values can be analyzed and compared within the image itself or between two different images.

OCT images can have varying texture due to the scattering properties of the sample being imaged. Different structure in the sample can cause the light to scatter in varying amounts and intensities. Speckle is another phenomenon that occurs in OCT images and can affect the image texture and pixel intensity values. Speckle could be noise or provide information about the sample. To analyze the OCT image texture, statistical methods can quantify the pixel intensities and provide information that describes how the texture remains consistent or changes throughout the OCT image.

When a tissue changes, many times the optical properties of the tissue are also altered. For example when normal esophageal tissue changes to Barrett's Esophagus tissue, the scattering properties change due to change in cells and tissue structure. Because the scattering properties of these two tissues are not the same,

these two tissues can be identified and classified based on the image texture. Structural analysis which evaluates the texture of an image by examining the patterns found in the image is not a useful method to use for tissue differentiation and classification. Because tissue does not have a repeatable pattern, the structural texture analysis method does not provide the information needed to evaluate the tissue. This section of the thesis will describe the statistical methods used to analyze the texture of normal esophagus and BE clinical images, and normal esophagus and BE phantoms. All images in this study were eight bit grayscale images, and have pixel values from 0 to 255. These statistical methods were applied in previous studies to differentiate and classify different tissue and clinical OCT images [12, 19-21]. Each method compares pixels throughout the image with a distinct process. A single method many times does not provide the information needed to classify or detect the necessary information an image therefore 2 or 3 different methods are used to evaluate image texture. Even though these statistical methods are distinct and use different algorithms, the same patterns or results are seen for normal and BE OCT images.

2.2 Texture Analysis Method - Speckle definition

Speckle is a phenomena that occurs when a laser beam is reflected back from a rough surface which causes the laser beam to have a spotted and uneven waveform [22]. The rough surfaces when moved causes a change in the reflected pattern of dark and bright spots of the laser beam even though there is no relationship between these dark and bright spots, and the texture of the surface[22]. This speckle, which is dependent on the optical properties of the sample, occurs because

of random interference between reflected waves, which are coherent. The light source, multiple scattering and phase aberrations of the propagating beam, and detector can also cause speckle to occur[22]. Both the tissue properties and system properties contribute to speckle in OCT images. Some speckle such as the speckle due to the system would be considered noise and should be eliminated when processing the signal. This speckle is typically a single pixel wide and can be reduced using different hardware and image processing techniques[21]. This type of speckle is not the focus for this project. Speckle due to properties of the sample can provide information on the sample. Speckle from the sample can be consistent in the OCT images and at the same location in the sample[21].

In OCT systems, speckle from the sample volume can occur whenever backscattered light waves from the sample interfere with each other and are received by the detector. These waves can be out of phase but still within an interval of time less than the coherence time of the source. The ideal signal for OCT imaging is a single backscattered wave of light from one scattering component from the sample only. This single backscattered light signal is difficult to obtain in tissue. Tissue is composed of a densely packed scatters, and some backscattered waves from multiple scattering centers combine to create an interference signal. Speckle can also occur because light can be reflected from different facets of a large component[22]. Subwavelength size particles contribute a large part of the optical cross section and for this reason contribute to the speckle in the OCT image. Light waves can also interfere with each other outside the sample. When the waves interfere with each other, it causes areas of constructive and destructive

interference that appear in the OCT images. Because different tissue types have different scattering properties, these differences would also affect the speckle in the OCT images. Speckle can be used to differentiate between different types of tissue and also between normal and diseased tissue[20]. Changes in speckle from different tissue influence the texture of the OCT image, and can be analyzed using the texture analysis methods described in the previous section of the paper.

When two waves interfere with each other, on the OCT image, this appears as a higher intensity area when there is constructive interference or a lower intensity area when there is destructive interference. The size of the speckle interference in the image can vary based on how the wave interference occurs. The wave interference is dependent on the scattering components or single component. In 2006, Gossage et al created gelatin based phantoms which contained varying concentrations of 3 different diameter microspheres which were .49μm, 1.59μm, and 3.01μm. These phantoms were created to study the effects of speckle on the texture in OCT images[21]. The texture analysis was performed using the SGLDM and DFT method, which is described in section 2.3 and 2.4 of this paper. The results demonstrated that as the size and concentration of the microsphere increased there was improvement in the classification of the phantom. This result is expected because as the number of scattering particles increase there is an increase in the number of multiple scatters in the phantom and therefore more speckle in these images. It is also important to note that even the plain gelatin produced speckle in the OCT images. This experiment demonstrated that modulation of the gelatin speckle pattern by light backscattered from one or more microspheres causes

differentiation of the set of texture features[21]. The results and conclusions from Gossage et al can be applied to this work in creating the phantoms and comparing normal and Barrett's esophagus OCT images.

Speckle plays an important role in the texture of the image. As stated above not all speckle should be considered noise. Speckle is needed to create an accurate image of the sample. When the tissue changes from normal to abnormal tissue, this will also change the speckle in the image and this affects the texture of the image.

2.3 Texture Analysis Method - Center Symmetric Autocorrelation (CSAC) Method

Previous texture analysis studies have demonstrated that natural textures have distributions of various specific local patterns of texture which have abstract symmetrical forms[18]. These gray value symmetric and antisymmetric textures can be measured by computing the auto-covariance or auto-correlation of the center symmetric pixel values of a specified sized matrix[18]. The Center Symmetric Autocorrelation method evaluates a pixel to all the neighboring pixels around it. A 3x3 matrix window is used to calculate the variance (VAR), between-pair variance (BVAR), within pair variance (WVAR), and gray scale texture covariance (SCOV) for the pixel in the image[19]. Two other functions, symmetric variance ratio (SVR) and normalized gray scale texture covariance (SAC), are computed from the other four functions defined above.

g_2	g_3	g_4
g_1	g_i	g_1'
g_4'	g_3'	g_2'

Table 1 3x3 matrix used to calculate the different variance functions used in the CSAC analysis. "g_i "is the center pixel which is compared to all the neighboring pixels.

The following equations describe the functions listed above and how each equation evaluates the center pixel value to the neighboring pixel values.

$$u = \frac{1}{8}\sum(g_i + g_i')$$

$$VAR = \frac{1}{8}\sum(g_i^2 + g_i'^2) - u^2$$

$$BVAR = \frac{1}{16}\sum(g_i + g_i')^2 - u^2$$

$$WVAR = \frac{1}{16}\sum(g_i - g_i')^2$$

$$SCOV = \frac{1}{4}\sum(g_i - u)(g_i' - u)$$

$$SVR = \frac{WVAR}{BVAR}$$

$$SAC = \frac{SCOV}{VAR}$$

In the equations above, "g_i" is the center pixel that is being compared to "g_i'" neighboring pixels defined in the matrix shown in Table 1. "u" is the local mean value calculated for each 3x3 matrix being analyzed. The three variance functions analyze the image texture based directly on the grey values of the pixels. These functions are sensitive to noise[18]. The BVAR functions measures the residual texture variance in the image[18]. Residual texture can be defined as small scale repeated texture detail[23]. Within pair variance helps evaluate homogenous areas with sharp boundaries[23]. Total variance (VAR) is the addition of BVAR+WVAR.

Most of the VAR in an image is due to the within pair variance. The three variance functions provide local variance information. The gray scale texture covariance function (SCOV) is a measure of pattern correlation and local pattern contrast[18]. This function is not normalized and provides more texture information than the normalized correlation measure SAC[18]. Both the symmetric variance ratio (SVR) and normalized gray scale texture covariance function (SAC) are less sensitive to local sample variations then the SCOV function. The SAC function has a range of -1 to 1. In this project, once these functions were evaluated for the pixels, a histogram plot was created for each function to assess and compare the texture in two or more images.

The CSAC method was chosen to measure and compare textures for OCT images because this method was used in other research papers to assess the texture difference between normal esophagus and BE clinical images[12, 19]. This method does have some errors and cannot always distinguish texture types[18]. The functions can be sensitive to noise in the local sample variations, and local gray scale transformations. Because this method compares local pixels in the 3x3 matrix, which can be affected by noise or local transformations, these local measurements may not accurately represent the full image. Therefore other texture analysis methods are needed to analyze the OCT images.

2.4 Texture Analysis Method - Spatial Gray Level Dependency Matrix (SGLDM)

The spatial gray level dependency matrix or co-occurrence matrix is another statistical method that quantifies texture in images. Like the CSAC method described above this method also uses histograms to assess the distribution of pixel

intensity values. As stated in the name, SGLDM is a spatial histogram which is then processed using different functions to quantify the pixels distribution in the image. The SGLDM is a second order joint conditional probability density function[21]. This second order joint conditional probability density function can be expressed in the following mathematical terms:

$$s_\theta\left(i, j_{d,\theta}\right)$$

In this equation, i represent the pixel being evaluated, and j is the pixel that is d distance from i in direction θ. The spatial histogram is the probability of a pixel with one grey value being a distance away from another pixel value in a certain direction. The co-occurrence matrix has possible values for i in the rows and j in the columns. The value of $s_\theta\left(i, j_{d,\theta}\right)$ represent the number of times value i co-occurs with value j based on the designated spatial relationshipsd, θ [24]. In this research and analysis of images, co-occurrence matrix were created based on the d distance set at 1 and for $\theta = 0°, 45°, 90°, and\ 180°$. $\theta = 0°$ means the direction of progress was comparing pixel i to the right of that value. When $\theta = 45°$, i was compared to the right diagonal pixel value. There were four histograms created for each direction θ but the distance in each of these histograms was set at $d = 1$. Once the co-occurrence matrix is created, 3 different functions analyze these values to provide useful texture information. Energy, entropy, and contrast were functions that were calculated to provide a numerical value for texture in the gray scale image. The numerical value calculated by each function quantifies different texture features.

$$Energy = \sum_{i=0}^{L-1}\sum_{j=0}^{L-1}\left[s_\theta\left(i, j_{d,\theta}\right)\right]^2$$

$$Entropy = \sum_{i=0}^{L-1}\sum_{j=0}^{L-1} s_\theta\left(i, j_{d,\theta}\right)\log s_\theta\left(i, j_{d,\theta}\right)$$

$$Contrast = \sum_{i=0}^{L-1}\sum_{j=0}^{L-1}(i-j)^2\, s_\theta\left(i, j_{d,\theta}\right)$$

In the above equation, L is the number of gray levels in the image and as stated in the previous section, all images were 8 bit gray scale images.

The Energy function is calculated by summing the square of each value in the co-occurrence matrix. The function is helpful to determine and compare homogeneity in images. An image with more homogeneity would have a larger energy value, because when computing this function an image with more homogeneity would have more relatively high values in the co-occurrence matrix. A homogenous image would have higher values in the co-occurrence matrix because ideally there would be less co-occurrence of different value pixels and more of the same co-occurrence. By squaring these higher co-occurrence values, this function should have higher values for images with more homogeneity. The range for this function is from 0 to 1, and an image with a constant pixel value would have an energy value of 1.

Because the entropy function multiplies the co-occurrence matrix value to the log of that value, this function gives a higher numerical value to an image with more pixel variation in the image. The log value increases the smaller co-occurrence values so that images with more pixel variations have a larger entropy value. Therefore an image with a higher entropy value could be considered to have more

heterogeneity than an image with a lower entropy value.

Finally, the contrast function, which is also known as the inertia function, is another measure of the amount of intensity difference in close proximity of the pixel in question. This function would have higher values for an image with more changes in pixel variation. The function favors contributions from $s_\theta\left(i, j_{d,\theta}\right)$which are away from the diagonal $i \neq j$. If an image had the same pixel value throughout the image, the contrast for that image would be 0. Other functions are also available such as local homogeneity and correlation, but were not used in this research because these functions did not consistently provide useful texture comparison results.

The SGLDM is a useful method for assessing and comparing texture in an image because each function provides a single numerical result. The functions used to evaluate the co-occurrence matrix also contribute specific texture information, which is straightforward. As stated in the previous section, many times a combination of functions are needed to assess the texture of image, because one function will not lead to the correct analysis of the image. This is also a reason to compute the co-occurrence matrix in different directions θ. There may be random patterns of large or small pixel value intensity in one direction, but overall throughout the region the change in pixel values may be more consistent. Both of the above described methods are based on statistics to analyze image texture. The next texture analysis method is not a statistical method.

2.5 Texture Analysis Method - Discrete Fourier Transform (DFT)

Two-dimensional Discrete Fourier Transform (DFT) is another method which can be used to analyze texture and pixel distribution in an image. In this method, the discrete pixel values in an image of size [MxN] are converted from the spatial domain $I(m,n)$ to the frequency domain $F(x,z)$.

$$\boldsymbol{F(x,z) = \sum_{m=0}^{N-1}\sum_{n=0}^{N-1} I(m,n)e^{-j\left(\frac{2\pi}{N}\right)xm}e^{-j\left(\frac{2\pi}{N}\right)zn},\ \ x,z = 0,1,\dots,N-1}$$ **Equation 1[19]**

Because these are discrete values and not a continuous function, the function is summed over the range of N instead of integrating over the space as done in a Fourier transform. Once the pixel values for the image are converted to the frequency domain, these values can be plotted. DFT can be used to detect periodicity and orientation in an image. In the plot, the edges represent the highest frequencies while the center represents the lowest frequency which is also the average pixel value. Images with more homogeneity would have a large proportion of lower spatial frequency signals. Images with periodic texture would have Fourier spectrums composed of significant peaks scattered in a consistent manner in some directions[25]. If the image has some type of direction texture such as horizontal lines, this information can also be observed in the Fourier spectrum.[25]. Images with random texture would have spectrum that is not restricted in to any direction.[25]

In this analysis, the Fourier spectrum was divided into four concentric squares based on the spatial frequency. The zero frequency

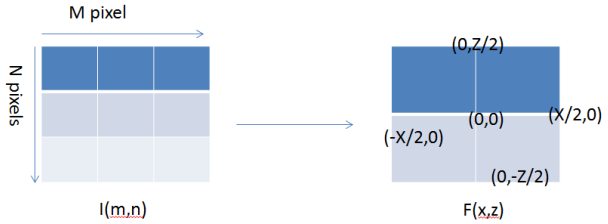

Figure 8 Diagram of going from the spatial domain to the frequency domain

component was shifted to the center of the spectrum.[19] The inner most square includes the lowest spatial frequencies while the outer most square had the highest frequencies. The magnitudes in each square were integrated and then divided by the total magnitude in the spectrum, which normalized all the spatial frequencies in the spectrum.

Analyzing texture with DFT is helpful because one can review the spectrum plot for information. The spectrum provides a visual diagram of the texture in the image. By converting the pixels from the spatial domain to the frequency domain, one can analyze the image for phenomena such as noise due to speckle or analyze the spectrum for patterns when analyzing similar images.

3.1 Methods Normal and BE Tissue Phantoms - Introduction

Barrett's esophagus (BE) is a condition in where the distal esophageal tissue changes to columnar mucosa. This intestinal metaplasia is confirmed with biopsies of the tissue. BE is considered a precursor to dysplasia which can then become cancerous in a small percentage of patients who have BE. Currently BE is detected during a white light endoscopy procedure. Many times it is difficult to see or locate BE because the change can occur just below the epithelial surface of the esophagus. Physicians do employ a procedure known as the Seattle protocol, which takes biopsies samples every 2cm in each quadrant of the esophagus. This method can miss areas with this condition because it does now allow the physician to inspect the full esophagus. It would be beneficial for physicians to have a method to visualize the full esophageal tissue below the surface of the epithelial layer.

Optical Coherence Tomography (OCT) is a novel optical imaging modality which can image 1-2mm below the esophagus epithelial tissue surface. OCT imaging can be used in-situ and produce real time, high-resolution micrometer images of the tissue structure. This imaging modality has the potential to improve detecting, monitoring, and diagnosing BE, and developing disease conditions such as low and high grade dysplasia, and cancer. OCT would enable the physician to complete a full examination of the esophagus. The physician could also visualize the esophagus below the surface where these conditions could exist, but are not visible under white light endoscopy procedures, or be missed when taking biopsies using the Seattle protocol. Researchers have analyzed normal esophagus and Barrett's esophagus tissue using OCT systems [12, 19, 26]. Some researchers have focused on

being able to visualize the tissue while other researchers attempted to develop algorithms, which can distinguish between normal and Barrett's esophagus[12].

Normal esophagus when viewed from OCT images, appear as a structured five layers of different tissue. BE lacks the five layer structure organization found in the normal esophagus. In BE, the epithelial layer is significantly thicker and two to three layers can be seen in OCT image. These layers in BE do not have the same visual characteristics as seen in normal esophagus. In addition, gland structures can be found in BE and the surface on the esophagus will not appear smooth and structured. These changes in the esophagus tissue are apparent in OCT images and histology. Because there can be much variability between OCT systems, these systems can produce different images from the same imaging site in the esophagus. There are some methods to evaluate OCT systems but many of these methods do not represent the environment of use. These basic phantoms and materials can evaluate the system performance and parameters, but as stated above, with systems being developed for specific uses, it would be beneficial to have a test method that represents the environment and characteristics of the tissue for the intended use of the system.

Tissue phantoms are constructed to represent and mimic specific properties of tissue. These phantoms can assess the performance of imaging systems. Phantoms can be created and tailored to function with a specific type of imaging modality. Because OCT systems can image in different organs and tissue types, it is beneficial to create phantoms that represent these organs, and assess these OCT systems performance for imaging these specific organs.

The purpose of this research is to construct phantoms, which represent the image texture, visual characteristics, and optical properties of normal esophageal tissue and Barrett's Esophagus when imaged by an OCT system. These phantoms will enable researchers to test new equipment and also compare results between systems. Researchers are developing phantoms for specific organs and tissue types because of the variability in optical properties and structure of the organs. Phantoms that do not mimic the properties of specific tissue are useful to assess some system technical specifications, but again the software and function of the system is many times designed for a specific organ, which these basic phantoms do not represent. Therefore using these unspecific phantoms do not characterize the performance of the system for that specific organ or tissue type.

3.2 Methods Normal and BE Tissue Phantoms - Material and Procedure for Phantom Construction

Many previous tissue mimicking OCT phantoms were constructed using a polydimethylsiloxane (PDMS, Slyguard 184) base [14, 16, 17]. PDMS is a transparent viscous liquid which when mixed with a curing agent solidifies. PDMS has an index of refraction of approximately 1.4. To create the image texture of the tissue, particles such as titanium dioxide (TiO_2) or barium sulfate ($BaSO_4$) are added to the PDMS base. These particles cause the light to scatter due to the index of refraction mismatch between the particles and the PDMS.

Before creating phantoms with PDMS and the scattering particles, a stock mixture was prepared. The stock mixture was created to have titanium dioxide (TiO_2)(anatase, Sigma Aldrich, St. Louis, MO) compose 10% of the total mass of the

PDMS based mixture. This TiO_2 had an approximate particle size of 5μm. PDMS and TiO_2 were added together and then mixed with a probe tip sonicator. The mixture was sonicated for over 12 hours with the sonciator set with a 25 second on cycle and 30 second off cycle. This initial mixture could then be diluted in a separate container, and used to create different concentrations of PDMS and TiO_2. Different concentrations of the mixture of scattering particles were studied to assess the effects on the image texture and scattering properties (Appendix 1). This assessment was considered in the development of different layers for the normal esophagus and BE phantoms.

To get the correct height for each layer, density and volume of PDMS was used to calculate the mass amount of PDMS to get correct depth. The area of the phantom was based on the size of a rubber washer. The rubber washer used in this research had an inner diameter of 2cm. Because the area was fixed by using a rubber washer, and the depth or height of each layer was also known based on the clinical information, the volume of the PDMS could be calculated. With the density and volume of the PDMS known, the mass of PDMS needed to create the correct layer height was then found. Once the PDMS, TiO_2, and curing agent were mixed together by hand, the mixture was placed in a vacuum pressure chamber for 20 minutes or longer to remove any air bubbles that may have formed during the mixing process. For the BE phantom, TiO_2 was mixed at specific concentrations to achieve the texture that resembles the top thicker epithelial layer in BE. For the first layer, TiO_2 composed .19% mass of the PDMS mixture. The percentage of TiO_2 needed to create the correct texture was based on previous work [10]. It was also

determined through trial and error and other research by Dr. Hsing Wen Wang a post-doctoral researcher at University of Maryland.

To create the rough surface found in many BE images, a 35AWG gauge copper wire of radius 143 microns was placed on a flat surface. The wire was cut to have a length of approximately 1cm. Glue was added to the ends of the wire to hold the wire on the surface. A glass slide with silane (SIO6715.5m Gelest Inc., Morrisville, PA) was used as the surface. The silane provided a hydrophobic layer, which was needed to remove the phantom from the glass surface after the curing process [9]. Another surface that was used in the process was Teflon block which also allowed the PDMS to be removed after being cured. A ring with a 2.00cm internal diameter was placed on top of the flat surface and around wire. The first layer of PDMS was then added on top of the wire. This ring ensured the correct area to allow the correct height to be formed. The first layer of this phantom should be 500-700um thick as seen in clinical images. Once the first layer was added on to the surface, glass beads were poured on to the phantom. A Pasteur pipette was used to add the glass beads into the PDMS mixture. The pipette allowed a small amount of beads to be released over the surface of PDMS and spread the beads over the surface. The glass beads (Polyscience Inc, Warrington, PA) 105-150um were added near the wire area. A specific mass or volume of glass beads was not measured. These glass beads would represent the gland like structures found in BE tissue. Because the PDMS was not solidified the glass beads could move to the middle or bottom of the PDMS layer. To help prevent the beads from moving to the bottom of the PDMS and settling on the surface, the surface was heated in an oven before

pouring the PDMS onto the surface and then adding the glass beads. Heating the surface also prevented the PDMS mixture from spreading and rising on to the ring used to create the area. The surface with the PDMS and beads was then put in the oven to cure the first layer. Once the first layer was cured, the second layer was added on top of the first layer. The second layer was constructed in similar manner to the first layer. As seen in the BE clinical images below, the structure and texture of BE is more apparent in the first layer. The second layer had less scattering particles then the first layer. The second layer was composed of .14% TiO_2. The second layer was constructed to be slightly thicker than the first layer approximately 600 -700um thick. The phantom was built with the 1st layer or epithelial layer on the surface against the wire. After both layers were cured and solidified, the phantom was removed from the surface. The phantom was turned over so that the side with the wire molding was now on top. The phantom was placed on a glass slide for the imaging process.

The normal esophagus phantom was constructed in a different manner than the BE phantom. Normal esophagus tissue does not have gland like structures in the tissue or rough surface tissue as seen in BE. The focus when creating the normal esophagus phantom was to construct the five layers of the esophagus. Each layer should have the similar thickness and visible properties as seen in clinical images. This phantom was constructed on a glass slide. Each layer of the normal esophagus is different in thickness as seen in the clinical images, but because of the different cellular structures, each layer appears to have different scattering properties. Blood vessels and other structure occasionally found in normal esophagus images were

not included in the phantom construction. Unlike the BE phantom, the normal esophagus phantom did not need to be constructed from top layer first and then removed and turned over. The bottom layer, muscular propria was created first, followed by the submucosa, muscular mucose, laminar propria, and finally the mucosal epithelium layer. After the first layer was cured, the following layer was added until all 5 layers were completed. Two different normal esophagus phantoms were created. One phantom was created using $BaSO_4$ (Sigma Aldrich, St. Louis, MO) scattering particles by Hsing Wen Wang a post-doctoral researcher at University of Maryland. This $BaSO_4$ also has an approximate particle size of 5μm. She used $BaSO_4$ scattering particles at different concentrations to differentiate each layer. The muscular mucosae (1% $BaSO_4$), submucosa (3% $BaSO_4$), muscular propria (1% $BaSO_4$), laminar propria (3% $BaSO_4$) and epithelial layer (2% $BaSO_4$) were constructed one at a time using spin coating to produce the different layers.

The second phantom was built with TiO_2 scattering particles which were also used in constructing the BE phantom. The muscular mucosae (.15% TiO_2), submucosa (.3% TiO_2), muscular propria (.15% TiO_2), laminar propria (.3% TiO_2) and epithelial layer (.23% TiO_2) were constructed one at a time by pouring the PDMS and titanium dioxide mixture on a glass slide. Because each layer is not same thickness, the mass of the mixture needed for each layer was calculated. The muscular mucosa was built to be around .5μm. The full muscular mucosae are not visible in OCT images. This layer was built thicker to also help prevent scattering from the glass slide in the image. The laminar propria and submucosa are about 200μm, which required .02g of the mixture. The muscular propria is slightly thicker

(250 μm) and was constructed with .025g of the mixture. Finally, the epithelial layer required approximately .07g of the mixture for a layer thickness of 300μm.

	Epithelial layer	Laminar Propria	Muscular mucosa	Submucosa	Muscular Propria
Percentage TiO_2 in PDMS mixture	.23%	.3%	.15%	.3%	.15%
Mass of mixture (grams)	.073	.018	.022	.02	.09

Table 2 Summary Of TiO_2 Scattering Particle Used for Normal Esophagus Phantom

	Epithelial layer	Muscular Propria
Percentage TiO_2 in PDMS mixture	.19%	.14
Mass of mixture (grams)	.2	.2

Table 3 Summary Of TiO_2 Scattering Particle Used for Barrett's Esophagus Phantom

3.3 Methods Normal and BE Tissue Phantoms - Optical Coherence Tomography (OCT) System and Imaging Procedures

The OCT system used in the study was a Spectral Domain (SD) OCT system which was custom built. The system had a center wavelength of 1315nm and a bandwidth of 85nm based on the full width half maximum of a pulse. A 10X magnifying lens (Thor labs) was installed on to the lens of the OCT system. The system had a theoretical axial resolution of 9um in air. The laser power output of the system was set to 7mW. This power output was from the lens of the system and not at the sample interface.

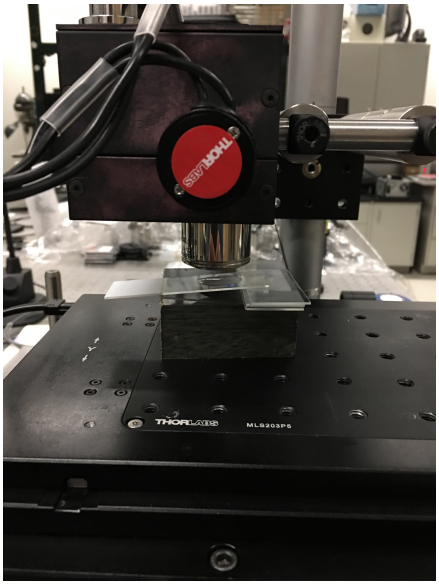

Figure 9 Imaging set up of Phantom

A 2mm line scan was used to image the phantom. This scan allowed for the features to be clearly seen in the image. This scan also appeared to be similar to scan lengths used in clinical procedures[20]. Unlike clinical procedures to image the esophagus, a probe was not used to image the phantom. The phantom was placed beneath the lens. The height of the phantom was adjusted so that the focus length was located 300-400um below the surface of the phantom. If the focus length is placed at the surface of the phantom, the images are not clear due to large index of refraction mismatch between the phantom and air. Multiple images of the phantom were saved and used for analysis. The height, or depth, of the phantom was measured optically with the system, and could also be measured by mechanical means. The overall depth of the phantom was measured using both optical methods and mechanical methods. The layers composing the phantom were only measured with the OCT system. Each layer of the phantom was measured optically with the goal that the layers would be the same thickness as actual esophageal tissue.

All images were 8 bit gray scale images. The images were created as bitmap files. The images were 564 pixels in width and 1024 pixels in height. The number of pixels did not change in the image when scan length was adjusted. From knowing the height of the phantom by mechanical measurement, and known number of pixels in that area, the pixel size was calculated based on this information. Each pixel represents approximately 4μm in height. The width of the pixel was computed by the known scan length (2mm) and the number of pixels in the width of the image (564). Each pixel was approximately 3.5μm in width. Images for analysis were cropped from the full image using the ImageJ image processing program. All images

were cropped to 118 x 118 pixels. This size was selected because it was large enough to contain the proper amount of texture information, but not so large that other unimportant parts of the image, such as the space between the lens and phantom, were not captured for analysis. The images were saved as jpeg files.

3.4 Methods Normal and BE Tissue Phantoms – Measuring Absorption and Scattering Coefficient

The optical properties, absorption and scattering coefficients, of the phantom were measured using an integrated sphere. The phantom was first placed in front of the sphere to measure the amount of light transmittance. To measure the amount of reflectance or scattering, the phantom was then placed in the back of the sphere. The optical properties were evaluated from the range of wavelengths of 1200nm to 1400nm. These wavelengths were chosen because the OCT system in this study had a center wavelength of 1315nm. Once the transmittance and reflectance data was collect for the range wavelengths, the absorption coefficient and scattering coefficient were computed using a MATLAB program. The optical properties of both the normal esophagus phantom and BE phantom were measured and calculated. The absorption and scattering coefficient of the phantoms were compared to the optical properties of the esophagus reported in the literature. The normal esophagus phantom data is shown in Figure19 and Figure 20. The modified scattering coefficient was found using an anisotropy (g) of .9 and $\mu_s' = \mu_s (1-g)$. Holmer et al measured the optical properties of the esophagus using an integrated sphere for a range of wavelengths from 300nm – 1140nm. These researchers reported an absorption coefficient range of .02mm^{-1} to 11.19mm^{-1} and scattering

coefficient of 5.94mm^{-1} at 1140nm. This comparison demonstrates that the normal esophagus phantom has a similar absorption and scattering coefficient as reported for a clinical esophagus sample using the same measuring method. At 1200nm, the scattering coefficient of the phantom is 6.5mm^{-1} and 5.94mm^{-1} at 1300nm. The phantom absorption coefficient of .019 at 1200nm is also similar to the clinical esophagus results. The optical properties of the BE phantom were also measured, but these properties were not expected. There is a significance difference in optical properties between the normal esophagus phantom and BE phantom. In addition, one would expect the modified scattering coefficient to decrease in the BE phantom due to the changes such as gland structure which were represent by glass beads and decreased concentration of scattering particles. The optical properties of BE from a clinical study was not available therefore these property results for the BE phantom could not be compared to BE tissue.

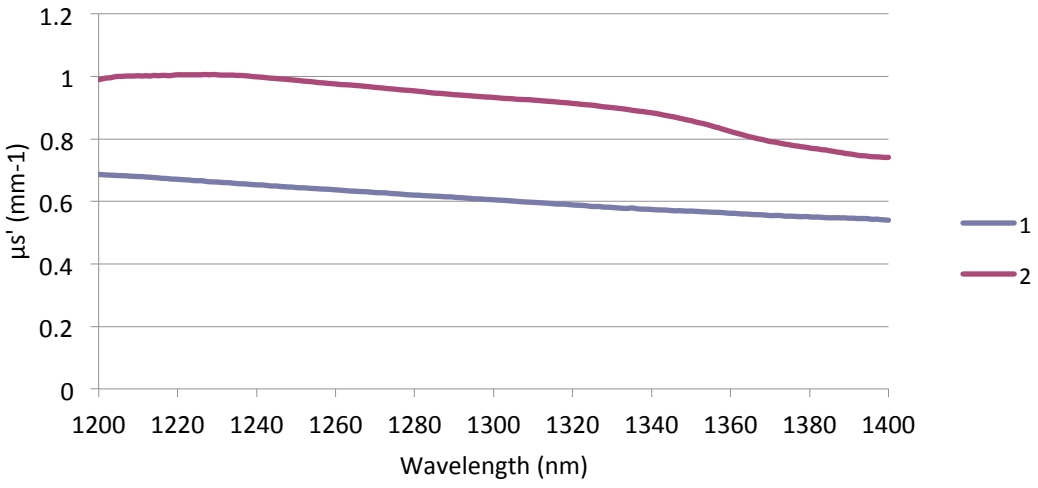

Figure 10 Scattering Coefficient of Normal Esophagus (Line 1) and BE (Line 2) Phantom

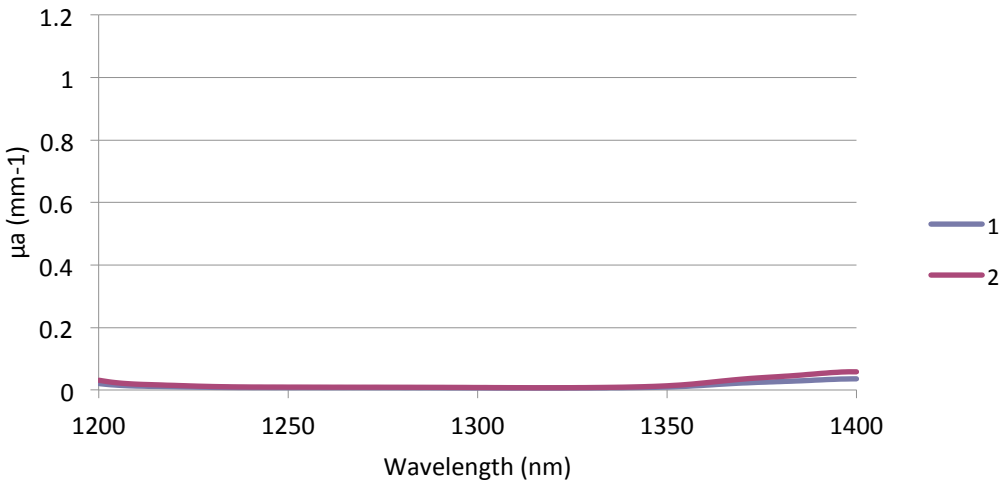

Figure 11 Absorption Coefficient of Normal Esophagus (Line 1) and BE (Line 2) Phantom

4.1 Results and Discussion – Visual Comparison of Phantoms to Clinical Images

After the phantoms were formed in the lab, the phantoms were imaged on the OCT systems. The normal phantom was observed visually for the layers. As expected, due to the concentration of the scattering particle, distinct layers are noticeable in the OCT image of the normal esophagus phantom. The layer thickness was also measured for each layer. No irregular structures were created during the process. The texture of each layer is consistent throughout the image.

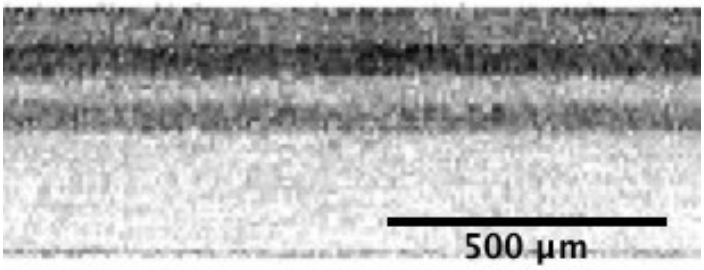

Figure 12 Image of Normal Esophagus Phantom

The BE phantom was imaged by the same OCT system as the normal esophagus phantom. As can be seen in Figure 12, the BE phantom has a thicker epithelial layer and a second layer. Gland like structure is visible due to the glass beads. Unlike the smooth surface on the normal esophagus, the wire molding created irregularities on the surface of the phantom. The layer thickness was also measured in the BE phantom. The BE phantom did have some shadowing from the gland structure, and high scattering areas from parts of the rough surface due to the interface with the air even with the focal plane set 200um below the surface of the phantom.

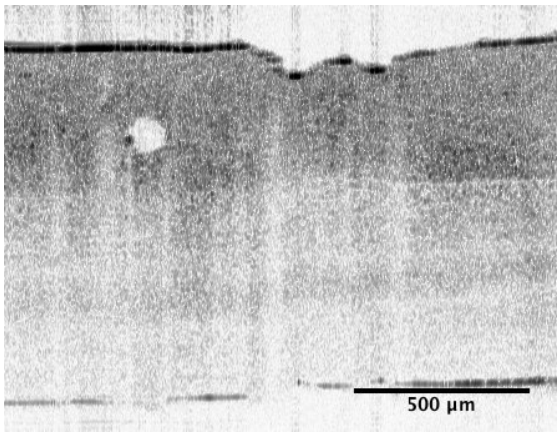

Figure 13 Image of BE Phantom

From the visual inspection of the phantoms, there is a clear and expected

difference between the normal esophagus phantom and BE phantom. From the visual images, both of these phantoms provide simulation of OCT clinical images of these types of tissue.

The phantoms do appear similar to the clinical images visually but it is apparent from the visual assessment that the phantoms do not exactly replicate the clinical images. Clinical OCT images of both normal esophagus and Barrett's esophagus were provided by Dr. Gullermo Tearney from Massachusetts General Hospital [27]. Figure 14 shows both a normal esophagus and BE clinical image and the normal esophagus and BE phantom. As can be seen in the clinical image, the layers appear to vary throughout the image, while the phantom image has a relatively consistent thickness throughout. Parts of the clinical image do appear very similar to the phantom image. The air-phantom surface interface is visible as a thick black line. This interface is not as prominent in the clinical image. For the texture analysis, the image was selected just below this interface so that it was not factored into the analysis. In both images, five separate layers are visible. The layers are not as

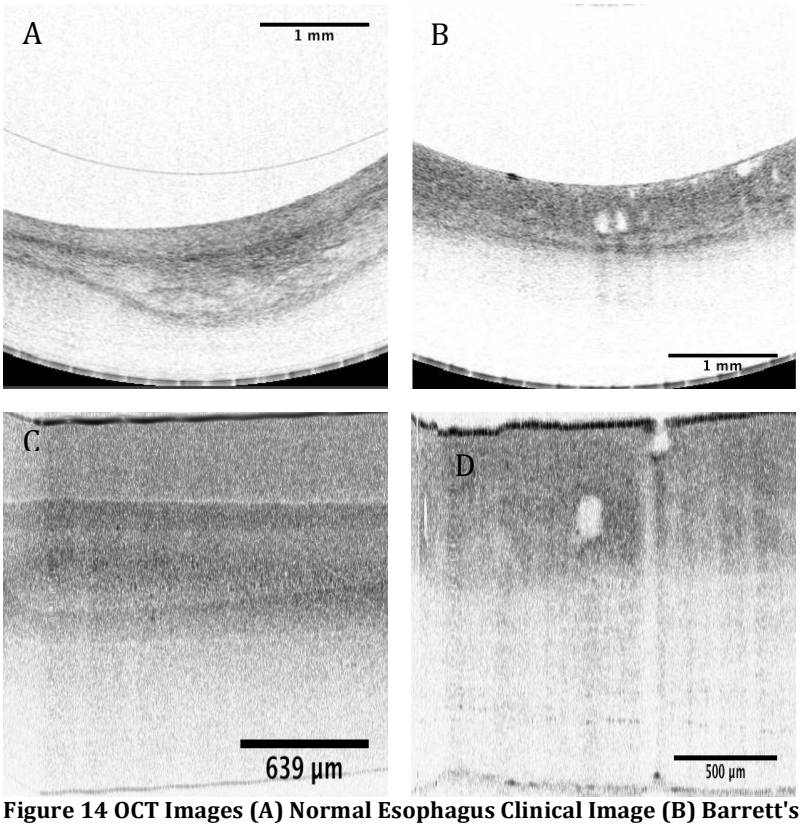

Figure 14 OCT Images (A) Normal Esophagus Clinical Image (B) Barrett's Esophagus Clinical Image (C) Normal Esophagus Phantom (D) BE Phantom

distinct in the phantom as in the clinical image shown above, but this is not always the case when compared to other clinical images. The left two images in Figure 14 show a clinical BE image and the BE phantom. Visually both of these OCT images do look similar. The surface roughness in the BE phantom does seem more structured than the roughness in the clinical image. The roughness in the clinical image is more random and not as organized in shape throughout the surface. The image texture for the first layer for both the clinical and BE phantom images are thicker than the layers seen in the normal esophagus, and with more irregular texture throughout the image. A visual inspection of the first layer in the clinical image texture does seem more irregular then the texture seen in the BE phantom. Both images show a shadowing affect immediately beneath the glands, occurring because of how the light transmitted, scattered and returned from these depths are affected by the gland structure above it. The glass beads are a good representation in size and optical effect as the gland structure in the clinical image. Gland structures are approximately 80-140um in diameter **[28]**. The second layer does not contain much information to discern change in the BE images. The second layer is accurately represented in the BE phantom image when compared to the second layer in the clinical image. Overall, visually the BE phantom does represent the clinical image better than the normal esophagus phantom represents the normal esophagus clinical images.

4.2 Results and Discussion – Texture Analysis of Clinical Images

To develop the normal and BE phantom, clinical images of both normal esophagus and Barrett's Esophagus needed to be characterized and analyzed. These images

were analyzed using the texture methods described above. Previous clinical studies have demonstrated that these texture methods can differentiate between normal esophagus tissue and Barrett's esophagus tissue [12, 19, 27]. Some of these studies applied an algorithm where the system identified Barrett's Esophagus based on the texture analysis of the images. This study does not attempt to create an algorithm to differentiate between normal and Barrett's esophagus images. This study does utilize the texture analysis methods to describe the differences in the image texture. All clinical images were processed before evaluating the images with the texture analysis methods. Part of the image were selected and cropped to a 118 x 118 pixel area using ImageJ image processing software. The texture analysis methods were all evaluated in MATLAB using custom programs. In all images, attempts were made to select the same axial area for analysis. The clinical images were analyzed to recognize how the image texture affected each function. Trends for normal esophagus images were observed and noted and the BE images were also reviewed for commonality between these BE clinical images. The normal esophagus and BE images were also compared with these texture analysis methods. These clinical image analysis outcomes were factored into the development of the phantom. The normal esophagus images show structure and consistent pattern of layers. When analyzed with all three texture analysis methods, there were fewer changes in local pixel intensities in normal esophagus images. The overall normal esophagus images were also found to have more homogeneity when compared to the BE images.

The SGLDM method showed that the normal esophagus images had lower entropy and contrast, and higher energy when compared to the BE images. These

results are expected because the entropy function is a measure of heterogeneity in an image while the energy function is measure of homogeneity in images. The contrast function, which is a measure of the intensity change from pixel to pixel, was not as consistent in demonstrating a difference between normal and BE images. Even though one would expect more intensity changes in BE images, there could be larger intensity changes between pixels in normal esophagus images. Because the pixel intensity changes in the normal esophagus images may be larger, these large changes can cause a higher contrast value then the multiple smaller pixel intensity changes that are found in BE images. These large changes in intensity could be found in areas of the image when moving from one layer to another layer. Overall, in most images analyzed, BE images had higher contrast then the normal esophagus images.

The SGLDM allows one to analyze multiple normal esophagus images and then compute an average and standard deviation of the normal esophagus images. The BE images are also evaluated using the same method. In this study, 5 normal esophagus images and 11 BE images from different patients were averaged for each function for 4 directions when analyzing neighboring pixels. The standard deviation was also calculated. The average and error bars representing the standard deviation were then plotted on a bar graph. This established a range of values for each function for normal esophagus and BE. In this research the Center Symmetric Autocorrelation (CSAC) method and Discrete Fourier Transform plots could compare one image to other single images, but the data from these methods could not be averaged and the standard deviation could not be computed with these

analysis methods, therefore these methods could not provide analysis of multiple images data in one plot or numerical value.

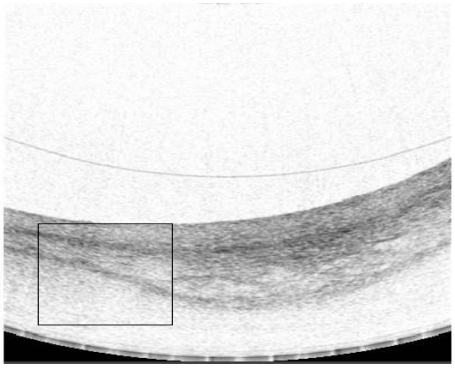

Figure 15 Example of full OCT image of the normal esophagus. Box in the image represents part of the image cropped for analysis.

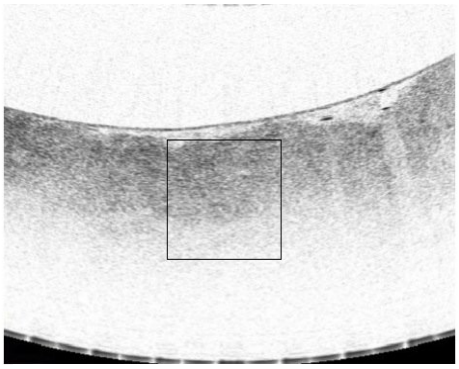

Figure 16 Example of Full OCT image of BE.

The Discrete Fourier Transform method converted each pixel value from the spatial domain to the frequency domain. These values were then plotted on a Cartesian plot with the zero frequency being the reference position. When evaluating normal esophagus images with DFT function, these images had a greater number of lower frequency components. The BE images were distinguished from the normal esophagus images because the BE plots have more high frequency values. As can be seen in Figure 10, the normal esophagus frequency values are more concentrated around the reference point while the BE images have more frequency values away from the reference axis. The DFT function demonstrated this trend when comparing the normal and BE images. All of the normal esophagus images did not have the exact same plot, and the BE images plot also were not identical. It was not expected to have the exact same plot when comparing the same type of tissue to each other. The DFT function demonstrated the trend that normal esophagus images had a higher concentration of lower frequency values, while BE images had larger range of frequency values including more high frequency values. Unlike the SGLDM method, DFT analysis does not provide as much description of the texture in the image. If patterns or lines were

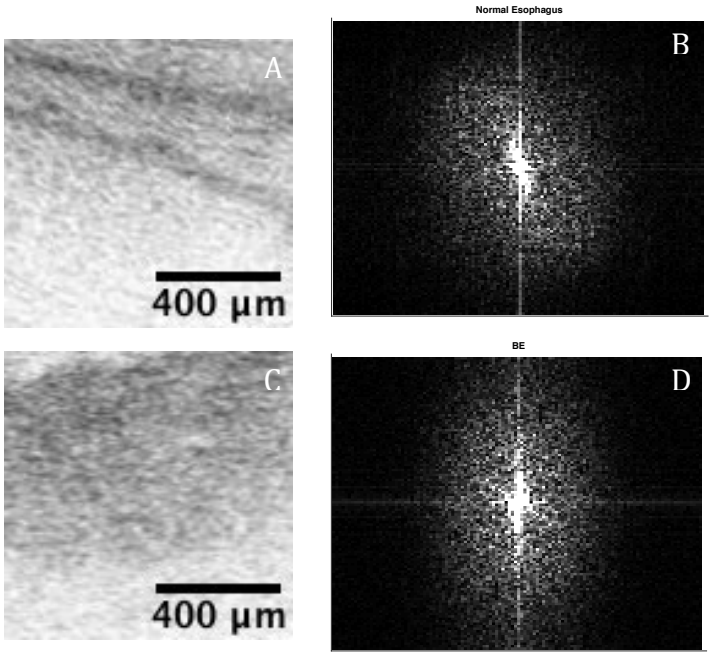

Figure 17 Normal Esophagus clinical image (A) DFT Plot of Normal Esophagus (B) BE Clinical image (C) DFT Plot of BE (D)

prominent in the image the DFT plot would be a certain shape [17]. The pattern of the plot would also be affected if the texture moved in a certain direction. For the clinical images analyzed, the clinical images did not have pronounced texture patterns or a direction for texture change throughout the image. The main benefit of using the DFT method, was the consistent differences between the frequency values in normal esophagus and BE image plots which can differentiate the overall texture in these images.

Textures of the images were analyzed using 6 different functions from the Center Symmetric Autocorrelation (CSAC) method. The first 3 functions calculated were the variance (VAR), within pair variance (WVAR) and in-between pair variance (BVAR). For these 3 variance functions, the normal esophagus images had a narrower range of for all three variance functions when compared to the BE images. These histograms show that there were less pixel intensity changes in the surrounding pixels in the normal esophagus images when compared to the BE images. The gray scale texture covariance (SCOV) function measures the pattern correlation and local pattern contrast in the image. Dividing SCOV function by the variance function derives the normalized SCOV (SAC). The SCOV function was one of the more consistent functions out of all the functions used. The normal esophagus images had higher correlation and less contrast according to this function. The symmetric variance ration (SVR) was calculated by dividing the within pair variance with the between pair variance. This function did not help in distinguishing between textures. The histograms in this method were not binned. The CSAC method is useful to analyze different aspects of the texture in the images

and to understand the texture difference in the two images. As with the SGLDM, in certain instance some functions in this method are more helpful in discerning the texture difference then the other functions. Some normal and BE clinical images were not discernable. In a few comparisons, the clinical images did not produce results, which were expected with some of the functions.

Even though the texture analysis methods were computed differently, all the methods showed that there were fewer changes in pixel intensities in the normal esophagus images. The energy function and the different variance functions would lead to the same conclusion. In addition the DFT method also demonstrated that when the pixel values were converted from the spatial domain to the frequency domain, the normal esophagus images had a larger amount of values closer to the zero value. The clinical images were analyzed to understand both the important visual markers and to quantify the texture in these images using the methods described above.

4.3 Results and Discussion - Phantom Image Analysis

These normal and BE phantoms were then compared to each other using texture analysis methods. The texture of the phantoms was analyzed to understand how the concentration of scattering particles, and material selection to create the phantom affected the image texture. The graphs in Figure 13 show the results of the Center Symmetric Autocorrelation method for texture analysis of the phantoms. These results, provided in Section 4.3, are similar to the results found in the literature for normal esophagus and BE clinical images [20]. Section 4.3 discuss and compares the phantoms to the clinical images. The three variance functions

demonstrated that the normal esophagus phantom has less change in local pixel intensity. The plots show a narrow range of variance for the normal esophagus images when compared to the BE images. This result would be expected when analyzing a pixel to the other surrounding pixels in a normal esophagus image because each individual layer has the same scattering properties. There should be less pixel intensity changes in these layers for the normal esophagus because these layers are of a single concentration of scattering particle and no glass beads or other structures are in these layers. The BE phantom would have more variation when comparing a pixel to the surrounding pixels, and structures like the gland and surface irregularity also add more changes both to the local image texture and overall image texture when compared to the normal esophagus. The symmetric variance ratio function was derived from the within pair variance and in between pair variance. This ratio did not help in analyzing the difference in texture for the normal and Barrett's esophagus phantoms images. As can be seen in figure 13, the plots were nearly identical and no trends were noticed when analyzing multiple images with this function. From the SCOV histogram, one can see that there is less contrast in the normal esophagus phantom images because it has a higher frequency of zero values in the histogram. These contrast results were also seen in the SGLDM contrast function. The normal esophagus phantom SCOV plot has a higher value in the correlation plot, which demonstrates there is a higher degree of pattern correlation in the normal esophagus images. The normalized SCOV (SAC) function also shows that there is less pattern correlation in BE phantom images when compared to the normal esophagus phantom images.

The SGLDM results also demonstrated a clear distinction for both the entropy function and energy function. The BE phantom had higher entropy and contrast, and lower energy values when compared to the normal esophagus phantom. Finally the DFT analysis also showed, that BE phantom had more high frequency values then the normal esophagus phantom, but the results were not as clear when looking at DFT plot for the different phantom images.

The texture analysis results demonstrate that the lower concentration of scattering particles increases heterogeneity. During the construction of the phantom different concentrations of scattering particles were evaluated to assess how the concentration of scattering particles affects the image texture. The BE phantom had a lower concentration of scattering particles then the normal esophagus. In addition, the glands and rough surface texture also contribute to the heterogeneous scattering. The texture analysis methods described in this paper are successfully able to distinguish the difference in these two phantom's textures.

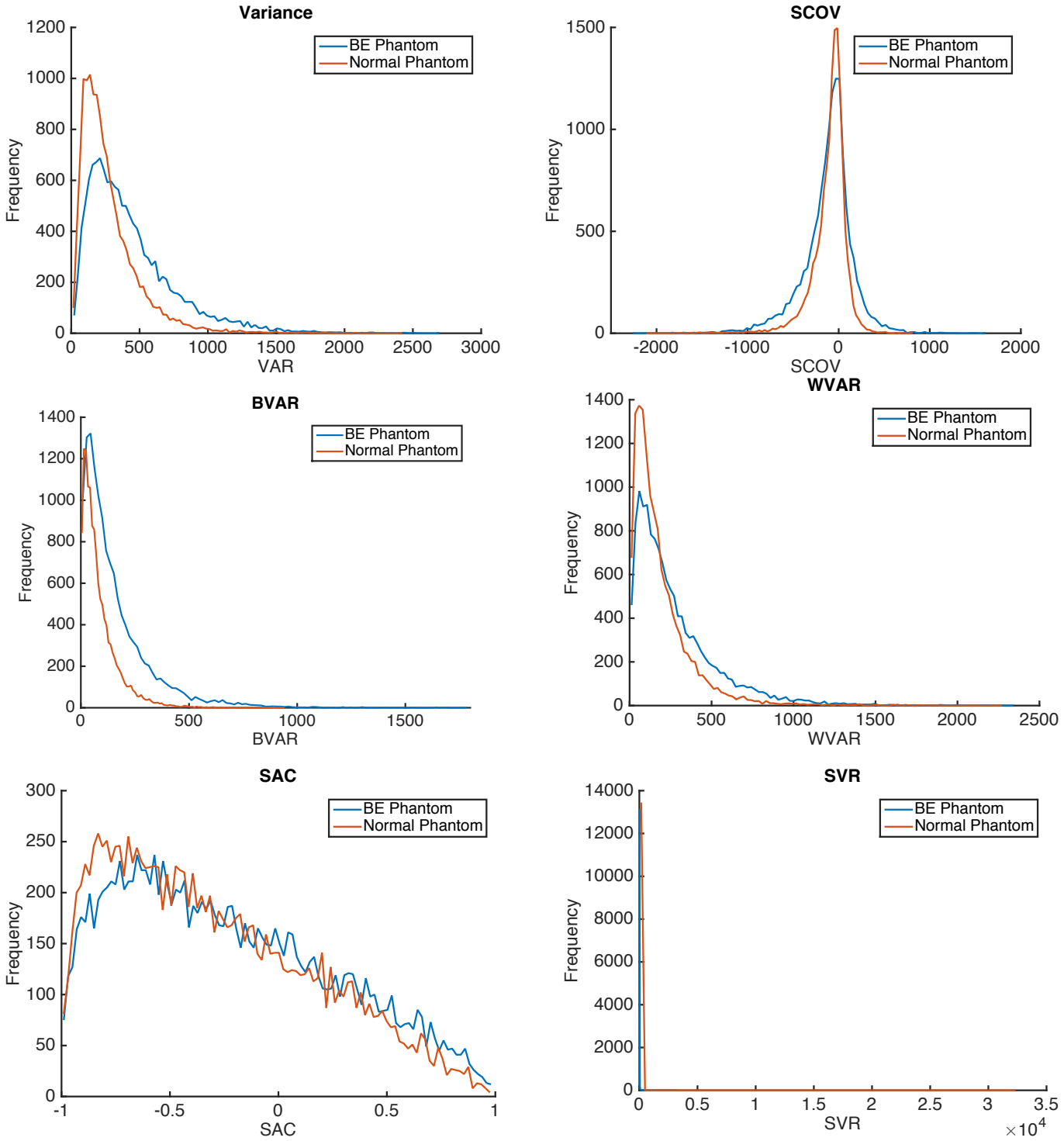

Figure 18 CSAC Texture Analysis Method for Phantoms.

4.4 Results and Discussion - Clinical and Phantom Images Comparison

The final part of the analysis was to compare the phantoms to the clinical images. Even though the two phantoms could be differentiated both visually and through texture analysis, these phantoms needed to be compared not only to single clinical images but also to multiple images to confirm that the phantoms have the same trend regardless of the changes that can occur in images of the same tissue type. These changes include varying layer thickness in the normal esophagus images, or the number and size of the glands in BE images. In addition, some of the traits found in the clinical images could not be included in the development of the phantom. These traits include the structure and specific lay out of the tissue found in the clinical images. It was important to also assess the effects of these differences on the image texture and was evaluated with the texture analysis methods.

The texture analyses of the phantoms to the clinical images were conducted in the same manner as described above for the other texture analysis comparisons. The same methods and functions were applied to assess the texture in the images. In addition to creating phantoms that are visually similar to the clinical images, the texture from the phantom images, when evaluated using these methods, should also demonstrate similarities as the texture in the clinical images. Because the visual assessment is a subjective assessment, the texture analysis methods provide a quantified outcome, and also evaluate how accurately the phantoms represent the normal esophagus and BE properties for OCT systems. As stated in previous sections, all images were 118 x 118 pixels. Figure 15 provides an example of the processed images utilized for the texture analysis.

The SGLDM results were used to compare both single images of the clinical image to the phantom. This method also allowed multiple clinical images to be evaluated, averaged, and computed a standard deviation for these images. Figure 15 shows the results of the phantoms being compared to multiple normal esophagus and BE clinical images. As previously described in the above sections, the results demonstrate that the SGLDM method is able to differentiate between normal and BE clinical images and between the normal and BE phantoms for all three functions which are analyzed in four directions. Each direction means that the pixel in question was compared to the pixel adjacent to it (0 degrees), the pixel diagonal to it (45 degrees), the pixel above it (90 degrees), and to the other diagonal pixel (135 degrees). Both the phantoms had more entropy, or heterogeneity, then the clinical images. The normal esophagus phantom did not compare well to BE clinical images using the texture analysis methods because the phantom did not fit the trend shown in the texture analysis between normal esophagus clinical images and the BE clinical images. Even though the normal phantom had higher entropy and contrast, and less energy than the normal and BE clinical images, it did compare favorable to the BE phantom. This trend was observable using all of the texture analysis methods. When using the SGLDM for single images the results were similar to the results provided below for the comparison with multiple images. Multiple

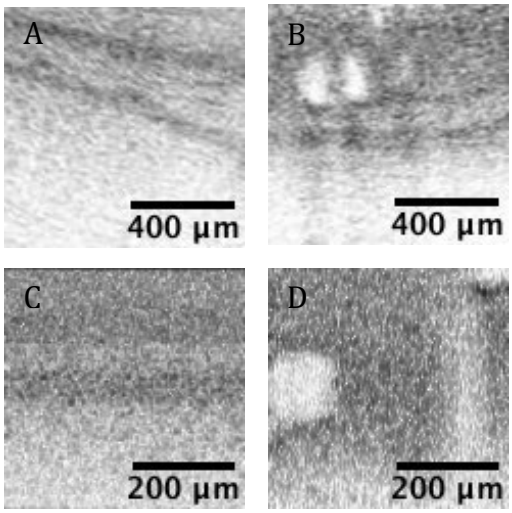

Figure 19 Example of processed images for texture analysis A) Normal Esophagus Clinical Image (B) Barrett's Esophagus Clinical Image (C) Normal Esophagus Phantom (D) BE Phantom

images from the normal esophagus phantom and BE phantoms were also used in the comparison. The results were also the same when taking multiple images from the phantoms and computing the average and standard deviation for those images.

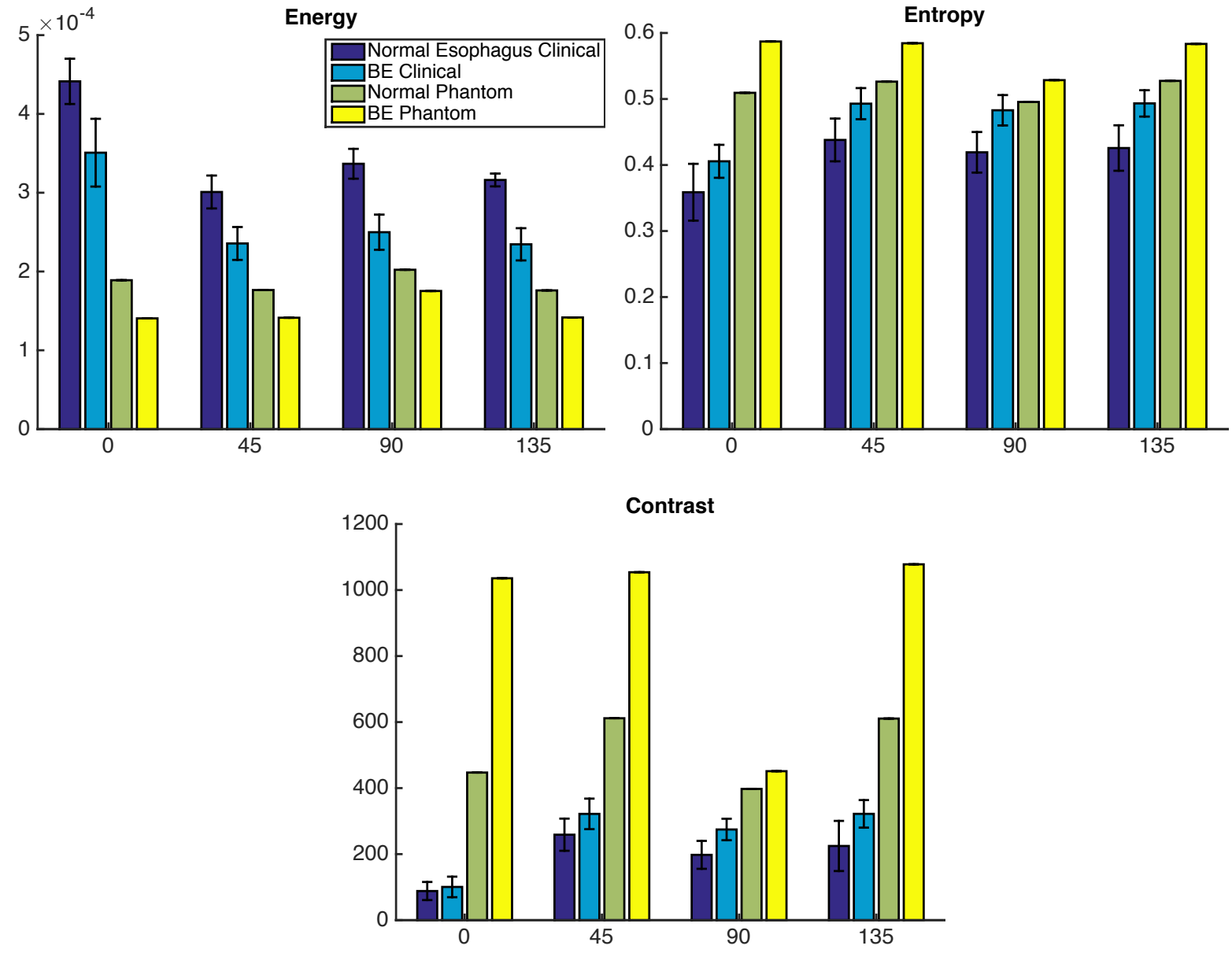

Figure 20 SGLDM Results comparing clinical images from multiple patients of normal esophagus and BE to the normal esophagus phantom and BE phantom.

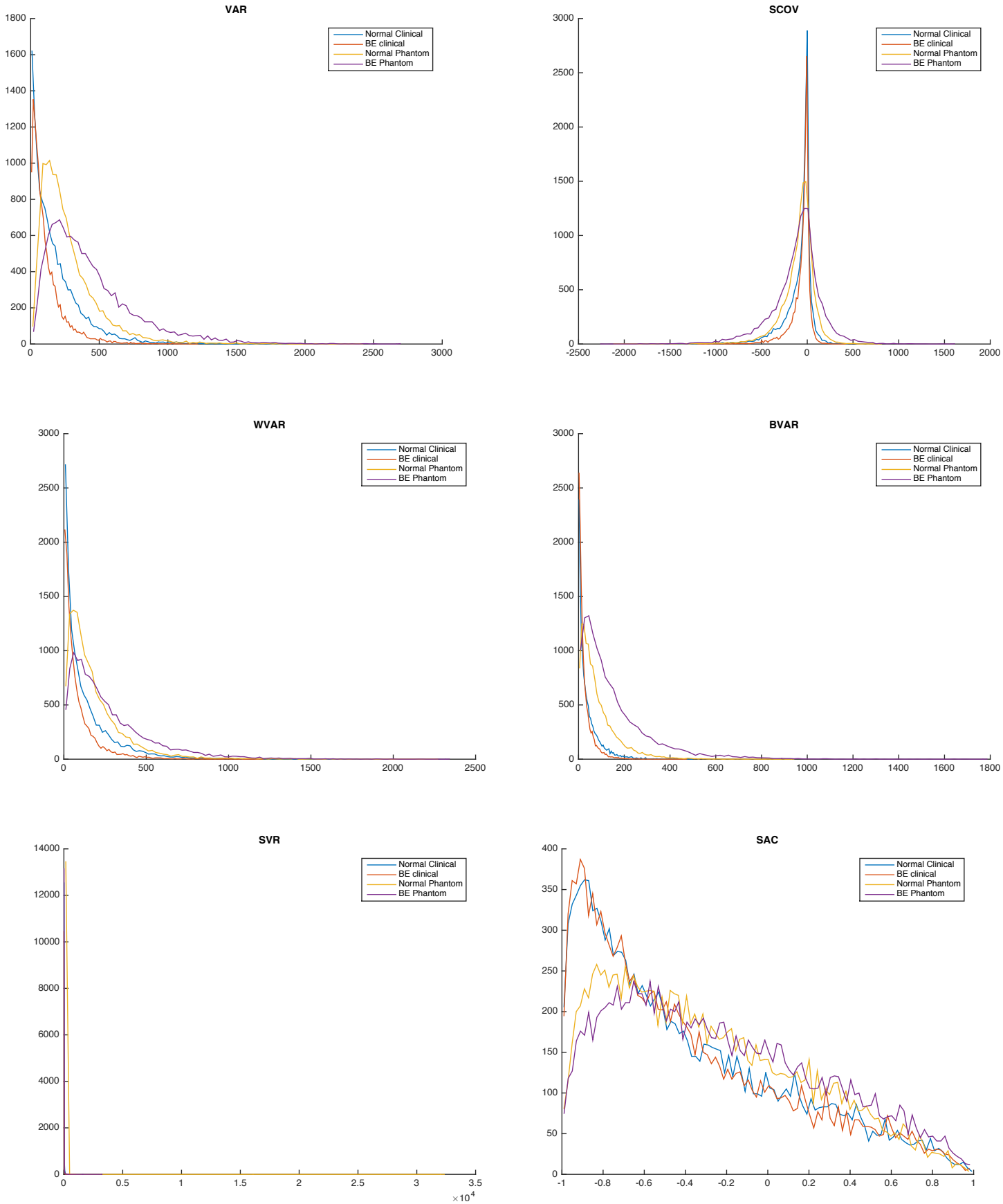

Figure 21 CSAC Results Comparing Esophageal Clinical Images to the Phantom Images

The CSAC method in Figure 17 showed similar results as the SGLDM. The clinical images had the same shape in these histograms. The phantoms had a different shape from the clinical images, but as shown in Figure(11) had similar shapes when compared to each other. Both the normal esophagus and BE clinical images had less variation then the phantoms. The SCOV function demonstrated that the clinical images had more pattern correlation then the phantoms. Again, though, the trend seen in SGLDM is also seen in the CSAC analysis for the clinical images and the phantom. Not all the functions in this method consistently showed the same results when comparing other clinical images. In some comparisons, the variation was higher in the normal esophagus clinical image than in the BE clinical image. The difference between the phantoms and clinical images were always apparent. The SCOV function was the most consistent function in distinguishing between the different images and had the same type of graph for most images. Overall this method was successful in demonstrating the same trends that were found in the SGLDM and in the analysis of the clinical images.

Finally, the DFT method was also successful in discerning between the normal and BE clinical images and phantoms (Figure 18). Like the SGLDM, the plot of the normal esophagus phantom was not ideal and had more high frequency values then the BE clinical image plot. Ideally the normal esophagus phantom would be similar to the normal esophagus clinical image and have less high frequency values then the BE clinical image. Regardless, this texture method again verified the trend found in SGLDM and the normal esophagus phantom could be distinguished in the same manner as the normal clinical images when compared to

the BE phantom.

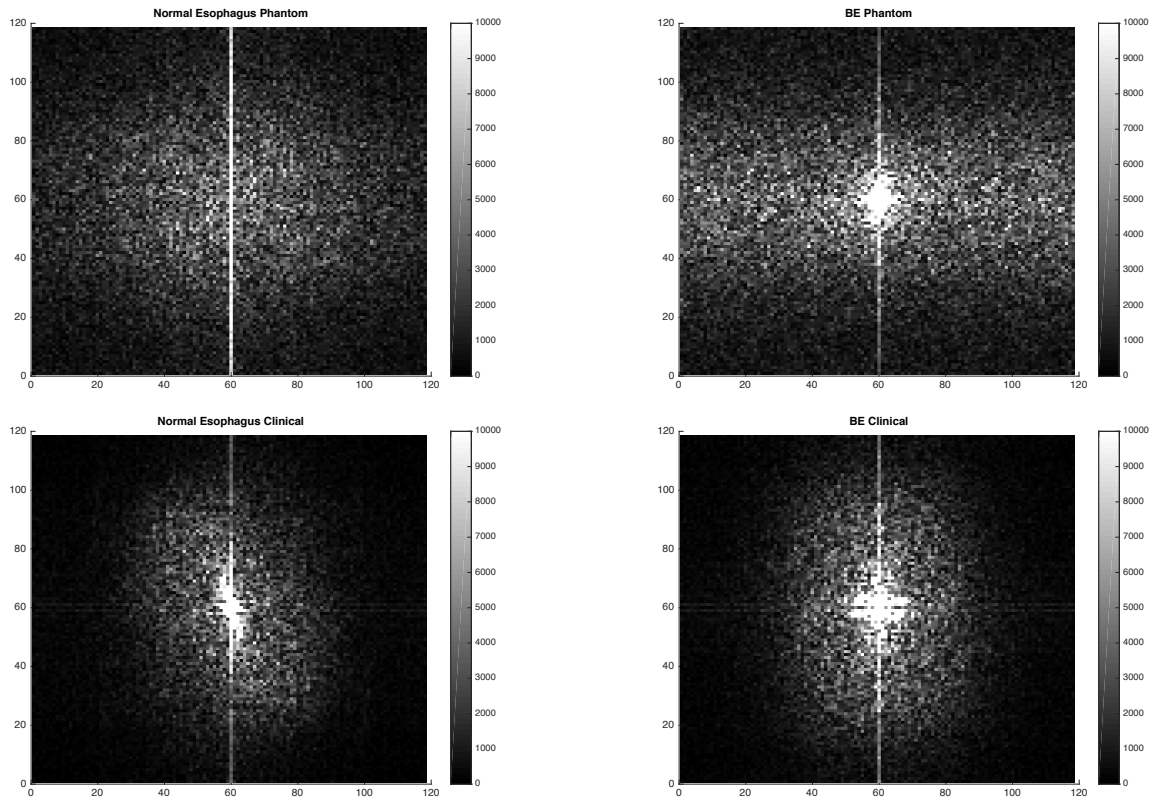

Figure 22 DFT Results of Clinical images and Phantom Images.

The three texture methods quantified the image texture for both the clinical images and the phantoms. Although the phantoms do produce images that visually represent normal esophagus and BE clinical images, there are some differences between the phantoms and images when evaluated using the texture analysis methods. Both the normal esophagus and BE phantoms had more pixel intensity variations then the clinical images. This is important because the goal is to create phantoms that are not only visible similar but also similar in image texture. The results from the analysis are positive in that both the normal esophagus and BE phantoms are discernable both visually and through texture analysis. The phantoms when compared to each other have the same outcomes and trends that

are found when evaluation the normal esophagus and BE clinical images. It appears, from this study, a range of values for each separate function from the SGLDM, CSAC, and DFT could be determined for the normal esophagus tissue and BE tissue. It does not appear that the other studies referenced in this paper focused on specific. By focusing on the individual functions, parameters could be determined for algorithms used to differentiation between normal and disease tissue. The research cited in this paper focused more on determining and differentiating between tissue types by using a combination of functions. Different functions could be used each time when analyzing and comparing images.

4.5 Results and Discussion - Future Considerations and Conclusions:

Phantoms have been constructed to mimic tissue properties [16, 17, 29]. The phantoms constructed in this research did mimic the normal esophagus tissue and BE, but there were some discrepancies when analyzed with the texture methods. The phantoms had higher heterogeneity and variability then the clinical images. Increasing the concentration of scattering particles could improve the texture but also negatively affected the visual image created. The phantoms in this research were modeled on clinical images that were taken with a different OCT system. It is unknown how these phantoms would be imaged on the system that produced the clinical images. It would be ideal to validate the phantoms on the same system that took the clinical images of the esophagus. Different systems can create slight differences in images. In a future study, it would be important to image the phantoms on separate OCT systems and evaluate the images from the two systems. Another important future consideration is to develop phantoms that include

characteristics of low grade and high-grade dysplasia. BE can be identified by OCT images, but it is just as important to monitor these areas for development of dysplasia which can lead to adenocarcinoma. The phantom would be a greater asset if it included this type of disease tissue. One would need to analyze the OCT image differences between esophageal tissue with dysplasia and BE before constructing these phantoms. Finally, for the phantom to be utilized with the different probes and simulate the environment for the OCT system, it would be ideal to develop a full esophagus model with normal and BE tissue. This model would allow for the OCT system and probes to be used as intended in the esophagus.

The goal of this research was to create phantoms that represent both normal and BE when imaged by OCT systems. When imaged with the OCT system, the phantoms produced images that mimic both the normal esophagus and BE visually. The normal phantoms had layers that were similar in texture to the layers in the clinical images. The BE phantom encompassed the heterogeneity, glands and rough surface found in the BE clinical images. With respect to texture the phantoms were not as accurate when analyzed by the texture analysis methods, but the same outcomes between normal esophagus and BE clinical images was also found between the normal and BE phantom. These texture differences could be attributed to the fact that the phantoms do not have as much random structures as the esophagus tissue. This research demonstrates that phantoms can be constructed and used to mimic the esophagus tissue when imaged by OCT systems. This work adds to the development of phantoms for OCT systems. These phantoms could help facilitate the development of OCT imaging systems both in the research phase and

performance testing of the device. This work should impact the analysis of phantoms by demonstrating the capability of texture analysis methods. In the future, these phantoms and analysis methods could be used to evaluate a systems performance and allow for one to assess the differences between OCT systems, probes, and software, which are under development to image the esophagus.

Appendix 1- Scattering Particles Characterization and Comparison to Clinical Images

The first part of the research required becoming familiar with the material used to construct phantoms. A literature study was conducted to understand the materials previously used to construct phantoms [15-17, 29, 30]. Previous, phantoms with the same desired characteristics of the esophagus phantoms were created using PDMS and scattering particles such as Titanium dioxide, Barium Sulfate, and Silicon Dioxide.

To have a better understanding of scattering material effects on texture, phantoms were created using only one scattering particle at different concentrations. The phantoms were then analyzed using the texture analysis methods described above. The goal was to understand how the different scattering particles affect texture at different concentrations. As stated in section 3, stock mixtures of scattering particles and PDMS were created. These initial stock mixtures were diluted to construct single layer phantoms of different concentrations. Once the mixture was diluted to the desired concentration with additional PDMS and curing agent, the mixture was placed in vacuum pressure unit to remove any air bubbles. The phantoms were then poured on to a glass slide and cured in the oven. Each single layer phantom was approximately 500-700μm thick. The thickness again was determined by the mass of PDMS added on to the glass slide. Once, the phantom was cured, the phantoms were imaged on the same OCT system described in Section Three.

	PDMS	Titanium Dioxide nanopowder	Titanium Dioxide	Barium Sulfate	Silicon Dioxide
Size of particle	N/A	20nm	5µm	5µm	40µm
Index of refraction	1.41		2.46-2.49 [15, 31]	1.636 (**National Center for Biotechnology Information. PubChem Compound Database; CID=24414, https://pubchem.ncbi.nlm.nih.gov/compound/24414**)	1.37-1.44[31] [15]

Table 4 List of Material Specification

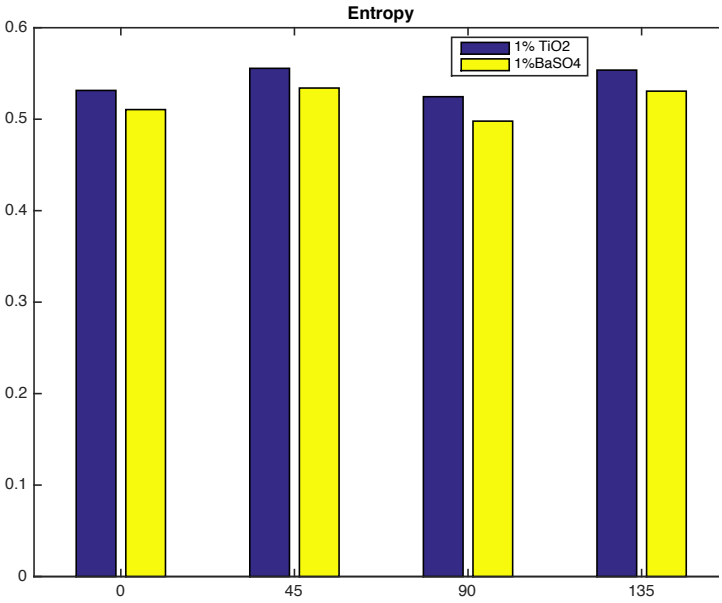

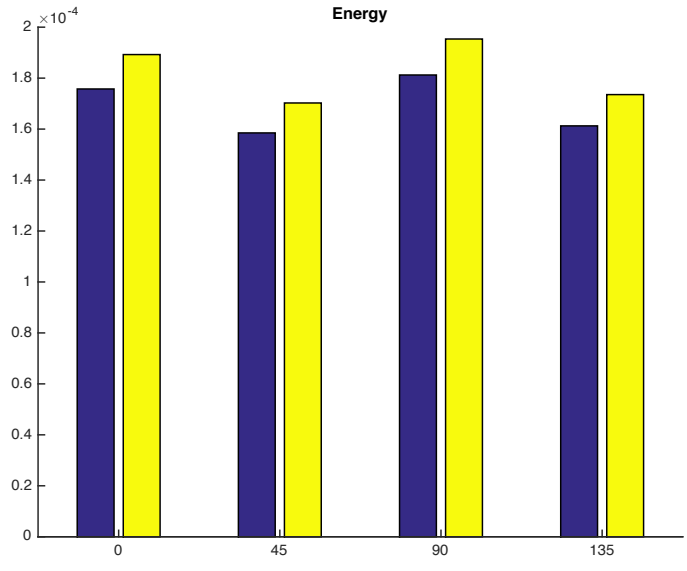

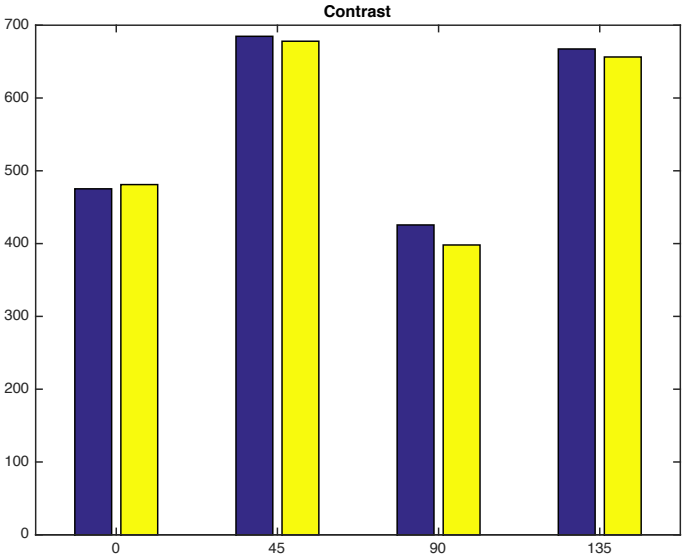

Figure 23 SGLDM Comparison of 1% TiO_2 and 1%$BaSO_4$

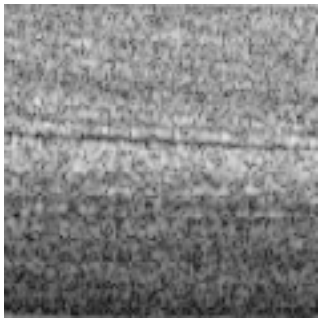

Figure 24 1% TiO_2 Phantom

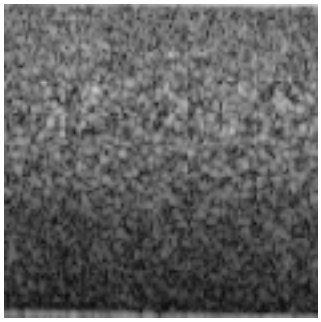

Figure 25 1% $BaSO_4$ Phantom

These SGLDM results comare 1% TiO_2 and 1% $BaSO_4$. The concentration and size of these particles are the same, but the refractive indexes of these particles are different. One would expect a greater change in texture between these two phantoms because of the differences in the index of refraction.

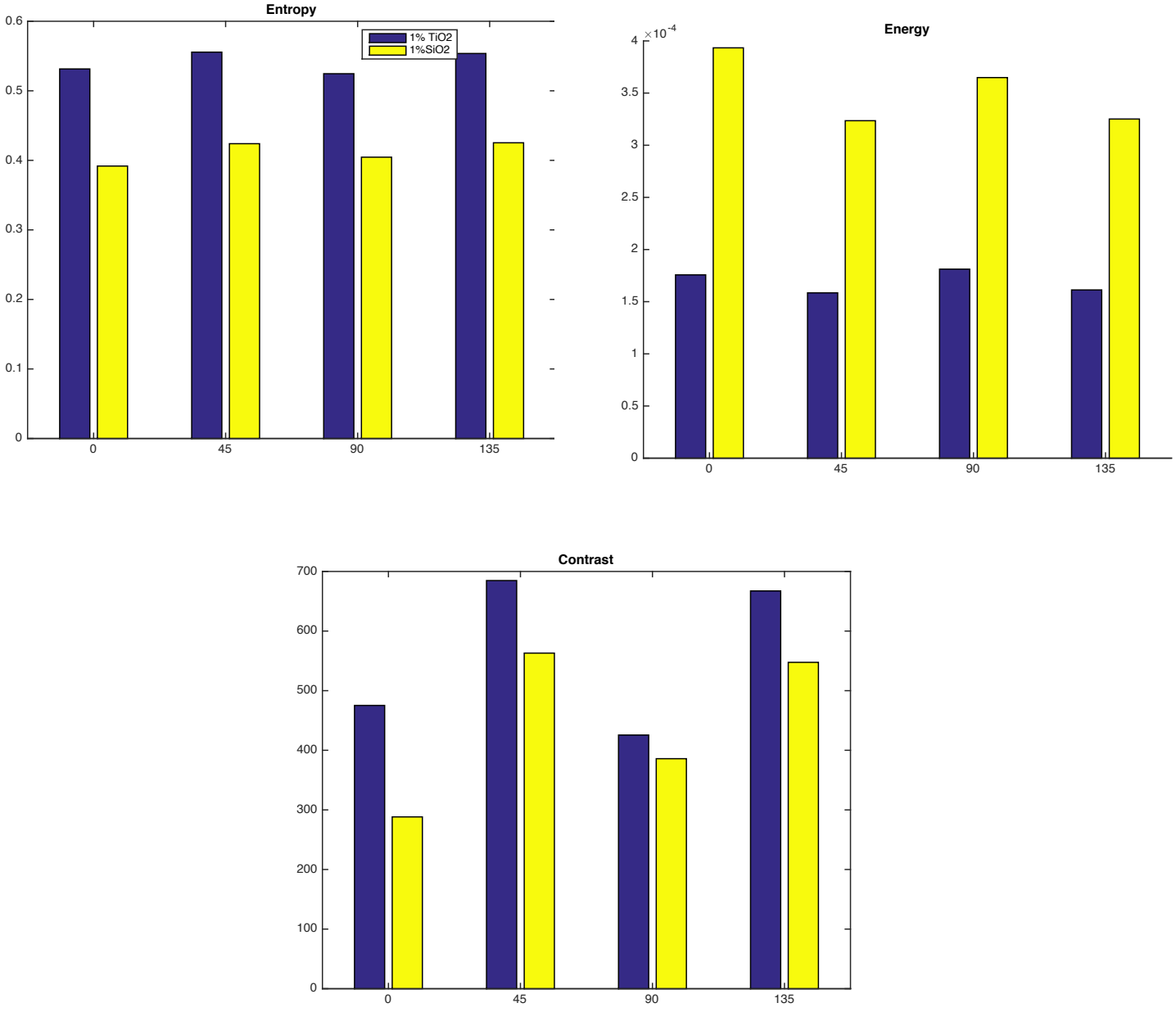

Figure 26 SGLDM Comparison of 1% TiO_2 and 1%SiO_2

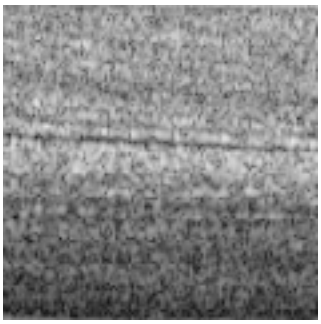

Figure 27 1% TiO_2 Phantom

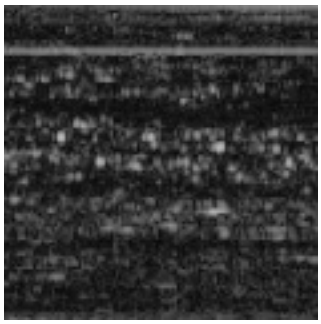

Figure 28 1% SiO_2

The results in Figure 24 compare TiO_2 and SiO_2 scattering particles effect on texture using the SGLDM. The silicon dioxide (U.S. Silica, MIN-U-SIL 40) had a particle size of 40μm. SiO_2 has an index of refraction, which is closer to $BaSO_4$. The size of the SiO_2 particles was bigger than the TiO_2 particles. It appears in these results that at the same concentration, the difference in index of refraction has a bigger effect on the texture results in the image.

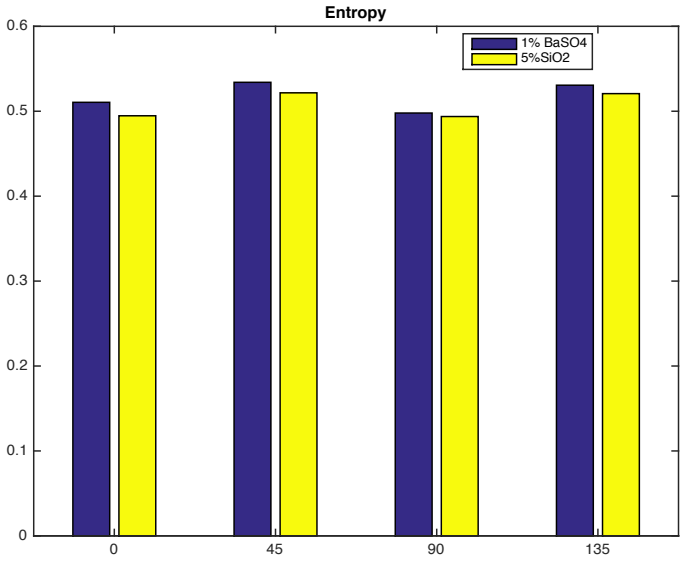

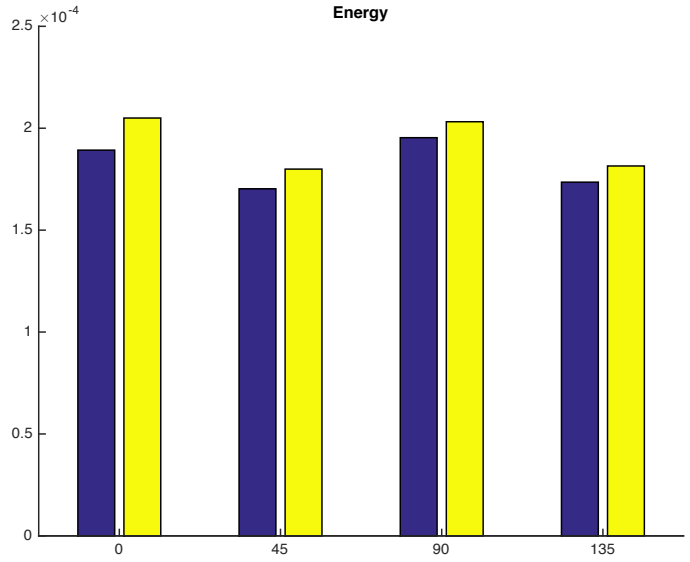

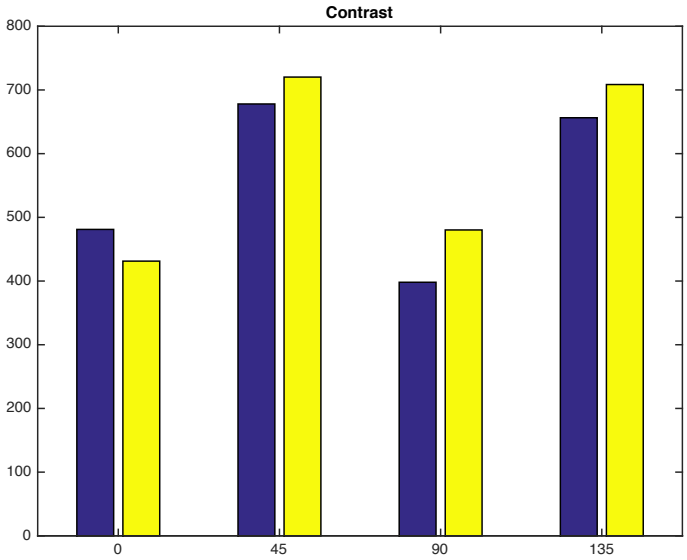

Figure 29 SGLDM Comparison of 1%$BaSO_4$ and 5%SiO_2

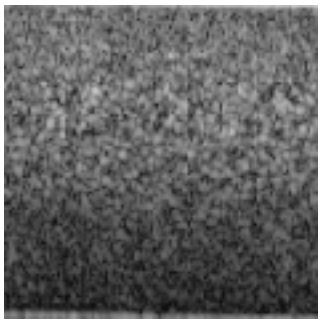

Figure 30 1%$BaSO_4$

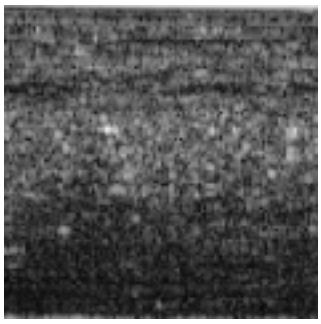

Figure 31 5%SiO_2

In this comparison, it appears that the 5% SiO_2 phantom has similar texture as the 1% $BaSO_4$. One could conclude that the increase concentration of SiO_2 particles has the similar results of the $BaSO_4$ particles, which has a higher index of refraction.

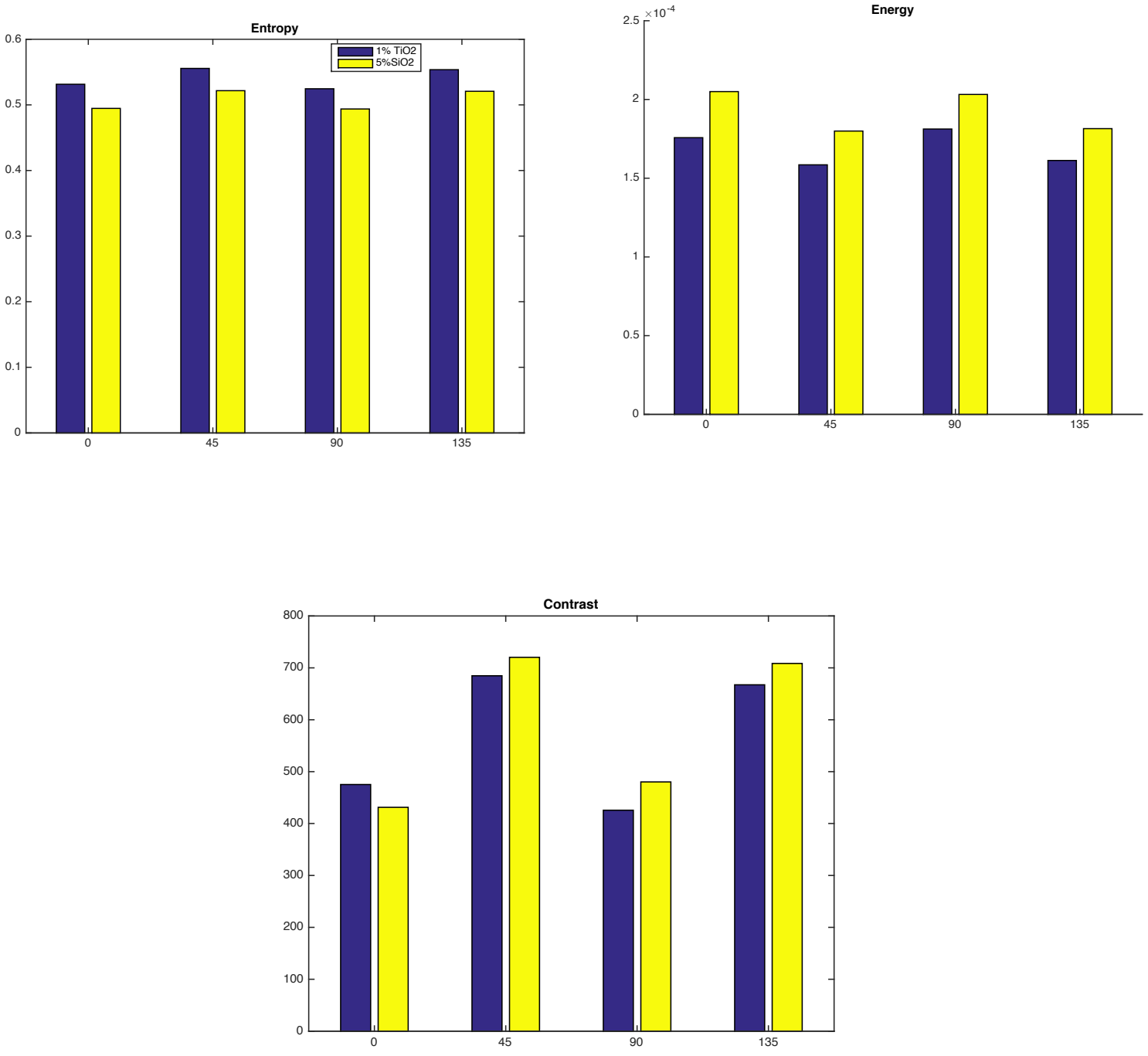

Figure 32 SGLDM Comparison of 1% TiO_2 and 5%SiO_2

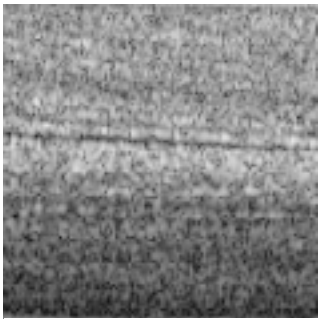

Figure 33 1% TiO_2

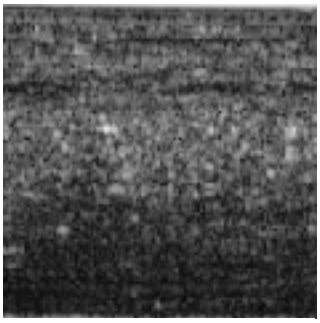

Figure 34 5%SiO_2

The SGLDM results in Figure 30 also support that at increase concentration the SiO_2 phantom starts to have similar texture as the TiO_2 phantom.

These single layer phantoms were also compared to clinical images (Figures 33 and 34). These comparisons were made to assess how the phantoms with different particles and concentration of particles replicate the tissue texture. TiO_2 was chosen to create the texture and visual aspects of the phantom. SiO_2 did not represent the tissue texture as well as the other two scattering particles. $BaSO_4$ was used in one of the normal esophagus phantoms. The BE phantoms and other normal esophagus phantom was constructed with TiO_2. There was more literature of phantoms that were created with TiO_2 [15-17]. These other research papers were referred to when deciding upon the concentration needed for the different layers of the phantom.

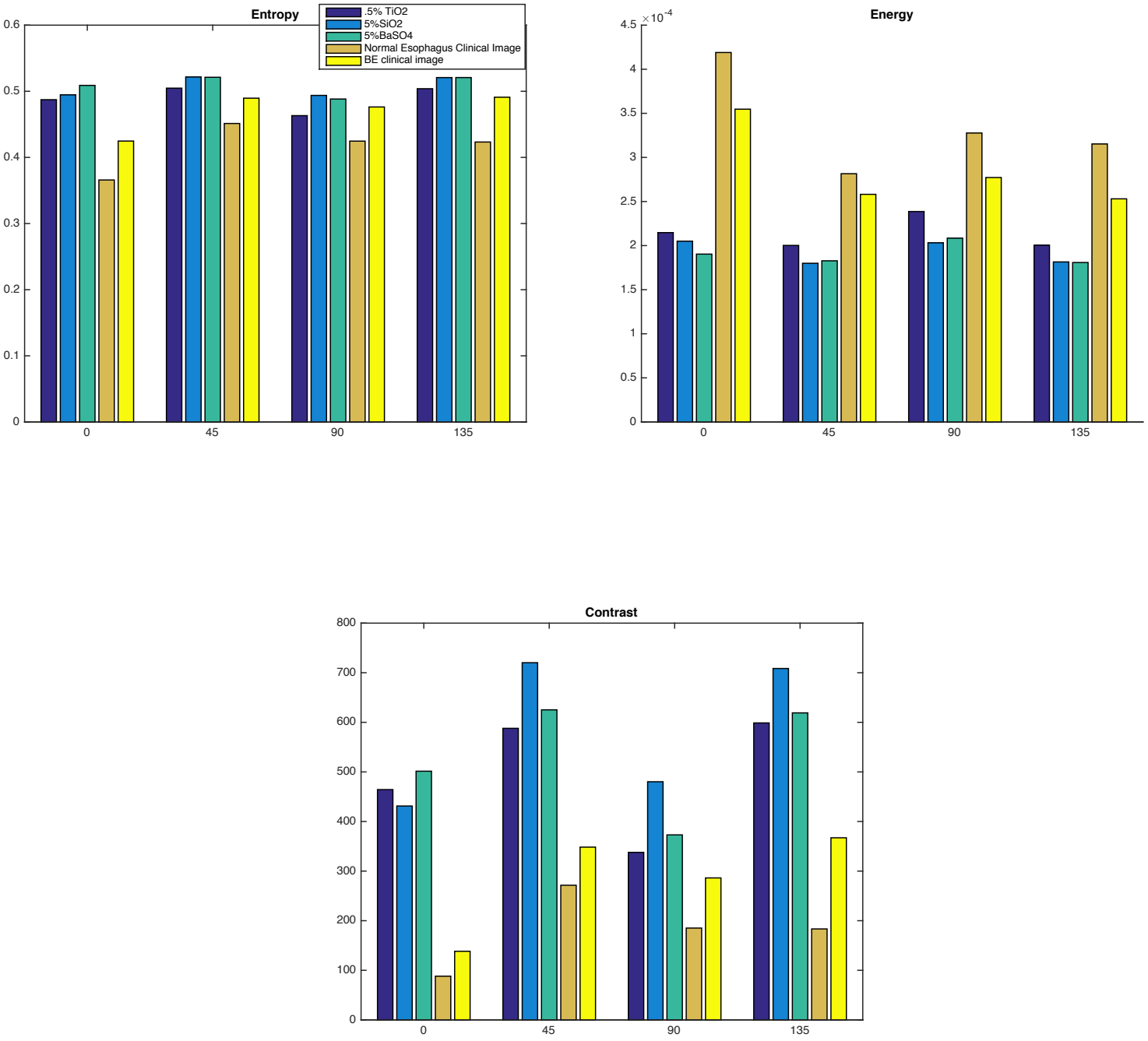

Figure 35 SGLDM comparison of .5% TiO_2 phantom, 5% SiO_2 phantom, 5% $BaSO_4$ phantom, Normal Esophagus Clinical Image, and BE Clinical Image

Appendix 2 – Scanning Electron Microscope Images

The particles were also imaged using scanning electron microscope (SEM). By imaging the particles, the size and the structure of the particles could be seen and understood. Three types of particles were imaged using the SEM system at the University of Maryland. Two TiO_2 particles were imaged. One particle was provided as nanopowder, and had the MSDS sheet stated the size of the particles were approximately 20nm. The other TiO_2 particle was the anatase and was reported to have a size of 5µm. $BaSO_4$ was also imaged. The manufacturer also stated that these particles were about 5µm. When the particles were imaged, the particles were not mixed with PDMS. A small amount of particles were placed in a container and then imaged by the SEM. The images from the SEM are provided below in Figures (14-16). The SEM images confirmed the size of the particles as provided by the manufacturer.

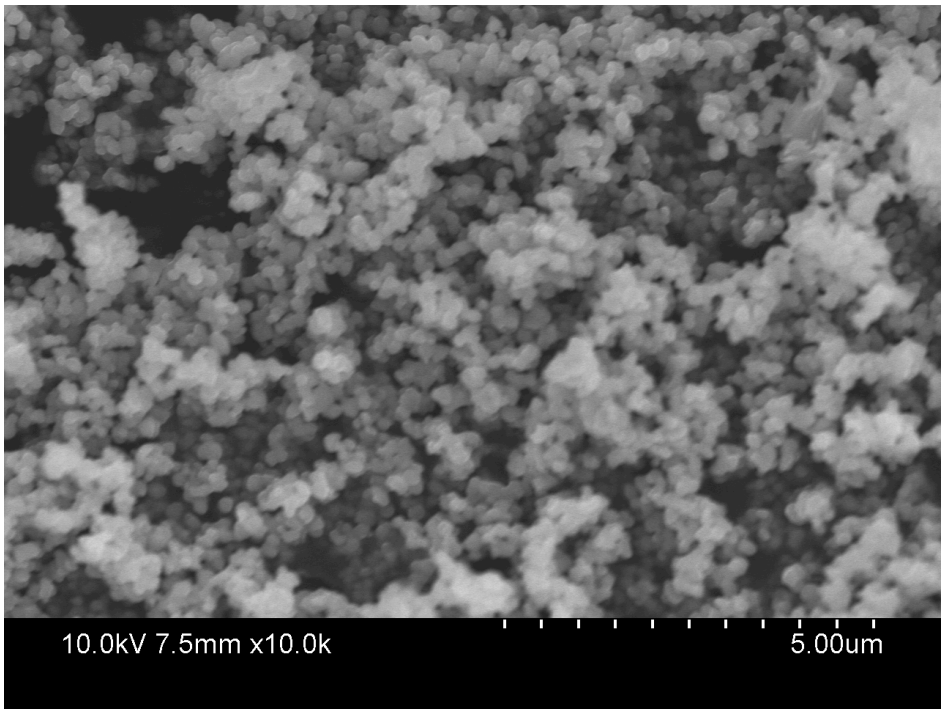

Figure 36 Image of TiO_2 Anatase Scattering Particles from SEM

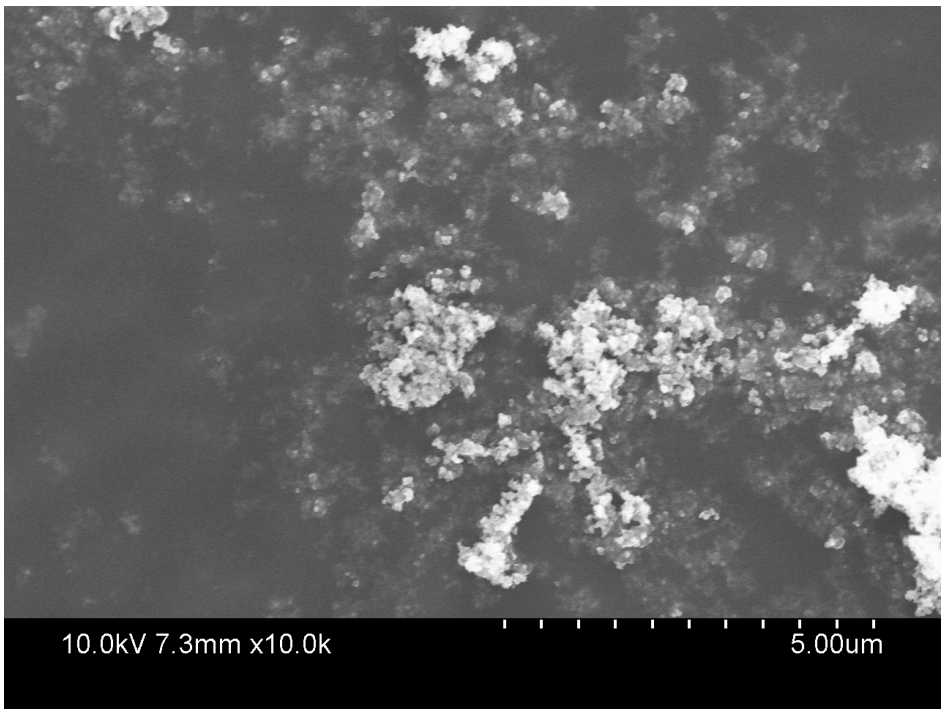

Figure 37 Image of TiO_2 Nanopartices for Scattering from SEM

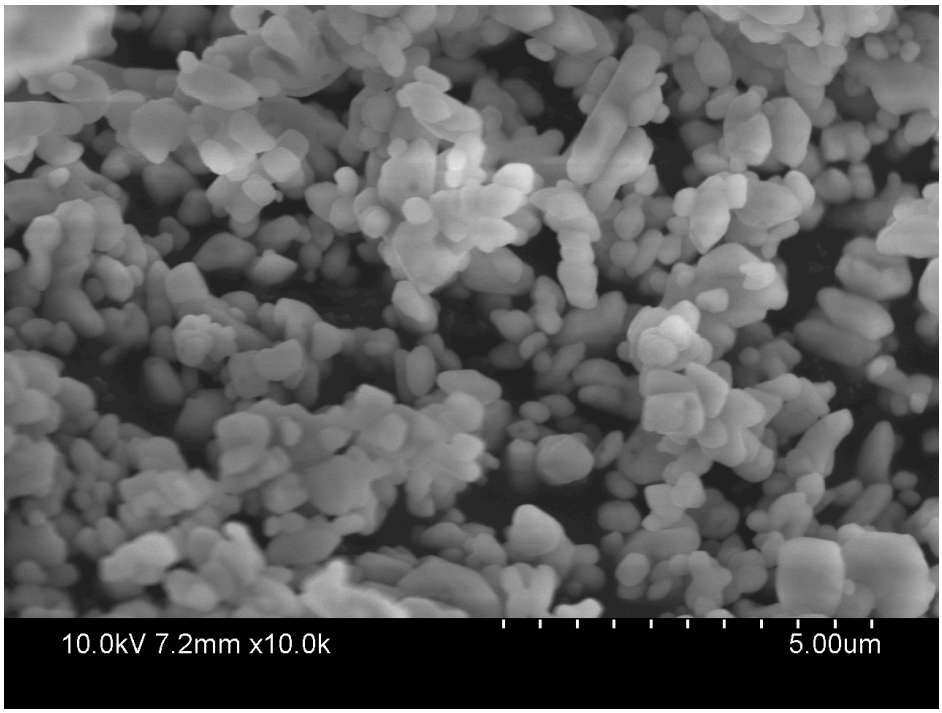

Figure 38 Image of $BaSO_4$ Scattering Particles from SEM

Appendix 3 Repeat Phantom Experiment with Gelatin and Silica Microsphere

Another experiment that was conducted early into the research was to repeat a previous experiment, which was published by Dr. Kirk Gossage in 2006[21] . In this experiment, Dr. Gossage was studying the effects of speckle on texture. As in the paper, phantoms were produced using 3 different size silica microspheres. Only one size microsphere was added in each phantom. The three sizes of microspheres used in the experiment were .5μm, 1.5μm, and 3.0μm. The phantoms were constructed of gelation and four different concentrations of the three sizes of silica microspheres. In addition, a plain gelatin phantom was also imaged. The four different concentrations of silica microspheres used in the phantoms were 500 million/mL, 100 million/mL, 25 million/mL, and 2.5 million/mL. The gelation powder was mixed in boiling water until the gelation had completed dissolved. The liquid gelatin was then mixed with the silica microsphere to obtain the right concentration. The gelatin and silica microsphere mixtures were then placed into a 24 count well plate. The well plate was placed into a refrigerator until the phantoms solidified.

The phantoms were immediately imaged using the OCT system described in Section Three. Each phantom was imaged several times from different areas of the well. The images were 564 x 1024 pixels using a 1mm scan pattern. The images were taken 300μm beneath the surface of the phantom. The images were cropped using ImageJ to be 128x128 pixels. The imaging method was performed differently than the method described in the published paper. In the paper, ten images of 512x512 pixel image of about 1mm in optical depth and 1mm in lateral extent were taken for each phantom. The images were then processed using the same method

described in the paper. The pixels were averaged to remove detector noise. Each image was now 64x64 pixels. To enhance speckle contrast, the images were further processed using a method called histogram equalization. This function is also available on ImageJ.

The texture from each image was analyzed using the SGLDM and DFT method. The texture analysis was also performed in a different manner than described in the paper. The researchers analyzed many more images and developed a classification software program using the SGLDM and DFT analysis data. The researchers did not examine the individual results from the functions of the SGLDM or the DFT. The developed program determined if one image was different to another image based on the results of the texture analysis results. The texture of the phantoms should have been different due to the different sizes of the silica microspheres. The size and concentrations of the microspheres should affect the speckle from the phantom and these changes in speckle should affect the texture in the image. The analysis in this researched focused on how the different size microspheres affected texture when analyzed by the functions in the SGLDM and DFT method. The individual functions were evaluated for trends when comparing phantoms with different size silica microspheres. The different phantoms compared the different size silica microspheres at the same concentration. For example, the .5μm silica phantom was compared to the 1.5μm at a concentration of 500million/mL.

In both experiments, the size of the silica microspheres was below the resolution of the OCT systems. As shown below, the results show that the size of the

microspheres affect the texture in the image. The functions that were most consistent in determining a difference in the texture of the images was the entropy and energy functions. The results from the paper are also provided in Figure (39). The results below show that as both size and concentration increase the entropy in the image increased and the energy decreased. It is important to note that the plain gelation was not transparent and also had some texture throughout the image Figure (38). As the concentration of microspheres decreased, the texture analysis results showed the functions becoming more similar to the plain gelation results. It was also more difficult to differentiate between images with the two size microspheres. When the 2.5mil/mL concentrations of microspheres were compared, the results also show that the texture becomes more similar. The purpose of this repeat experiment was to demonstrate and analyze how the size and concentration of scattering particles affect the texture due to the change in speckle. There were differences in how the images were analyzed. It does not appear that the paper focused on the results from the individual functions. The researchers used an algorithm to differentiate between phantoms. In this repeat experiment, no algorithms were created, and the emphasis was on evaluating each function when evaluating the texture. As the researchers concluded, it does appear that these texture analysis methods and functions can be used to differentiate between different phantoms that have different concentrations of scattering particles. This is relevant in analyzing normal and diseased tissue. Where the concentrations and size of the cells change when the tissue

It did appear that there were errors made when making the samples, which can be seen it the results. The texture analysis always showed a difference between the plain gelatin and the phantoms containing silica microspheres. In some of the comparisons, the expected results were not seen. These expected results were based on the texture results, which demonstrated in increase in entropy and decrease of energy when the size or concentration of microspheres increased. These errors were most likely due to the weighing and mixing of the silica microspheres with the gelatin solution. A small amount of silica microspheres were weighed when making the mixture, so an error or ±.01 grams could increase or decrease the number of microspheres in the solution especially as the size of microsphere decreases.

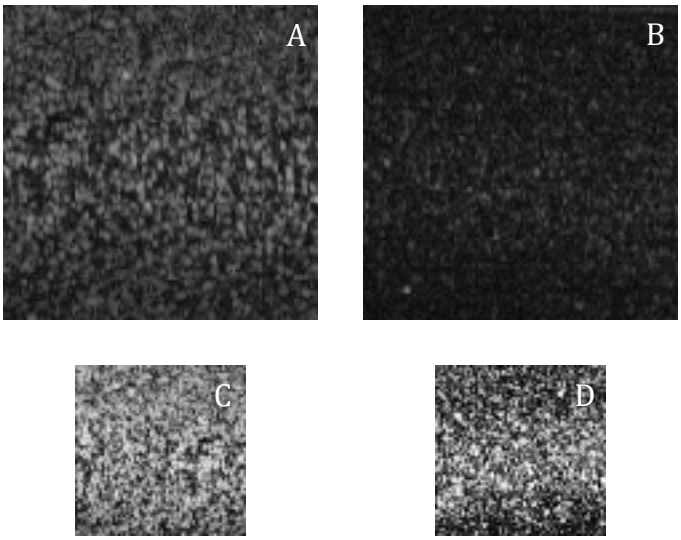

Figure 39 Unprocessed Image of 1.5um 500mil/mL (A), Unprocessed Image of Plain Gelatin (B), Processed image of 1.5um 500mil/mL (C), Processed Image of Plain Gelatin (D).

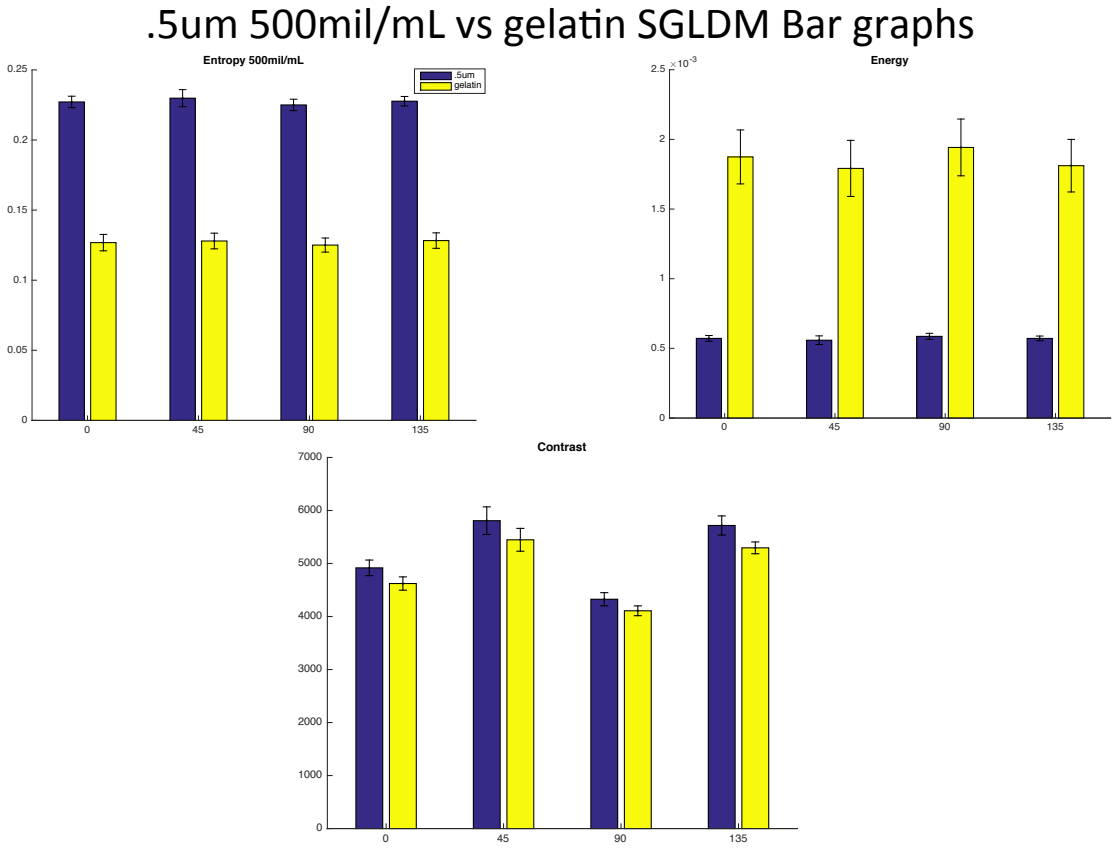

.5um 100mil/mL vs gelatin SGLDM Bar graphs

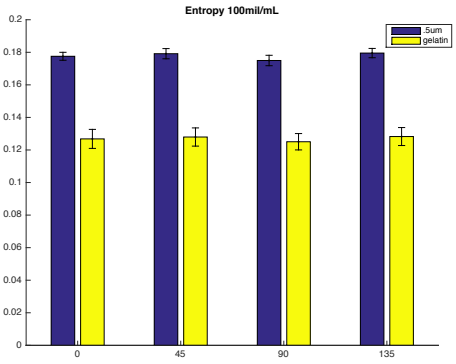

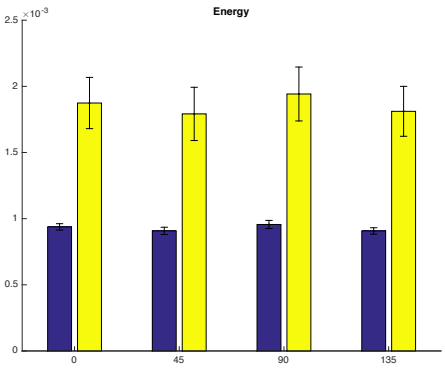

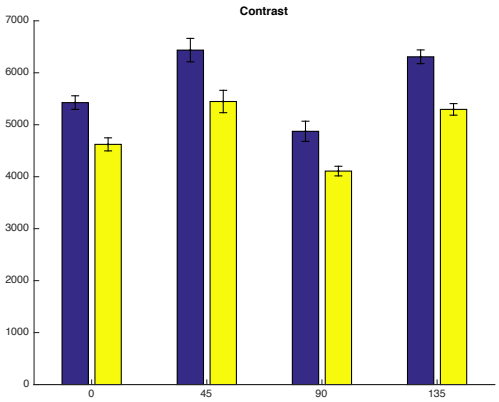

.5um 25mil/mL vs gelatin SGLDM Bar graphs

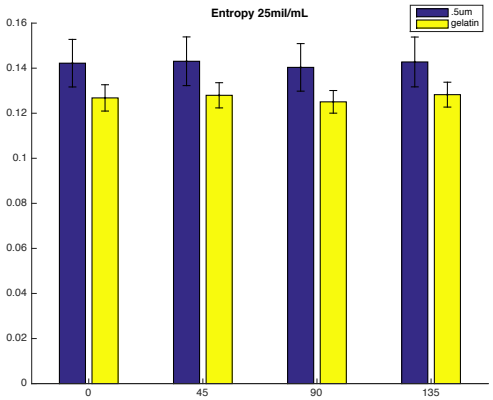

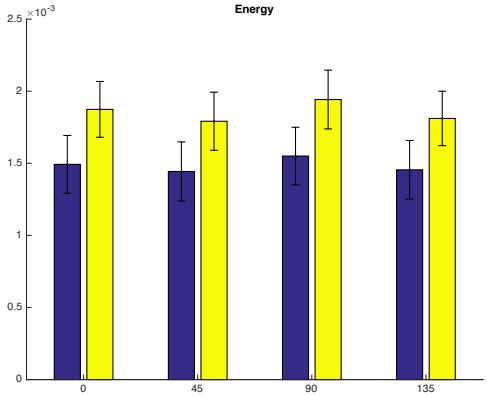

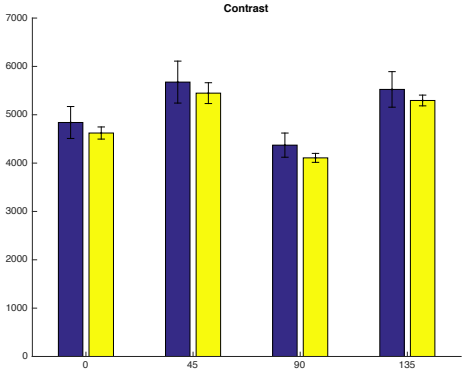

.5um 2.5mil/mL vs gelatin SGLDM Bar graphs

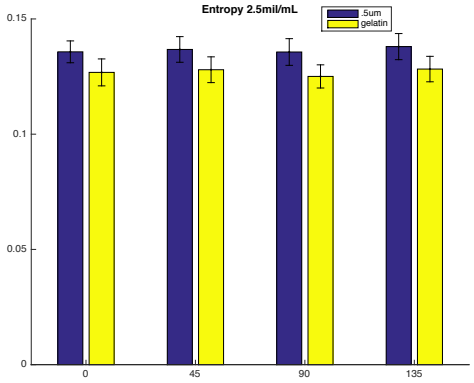

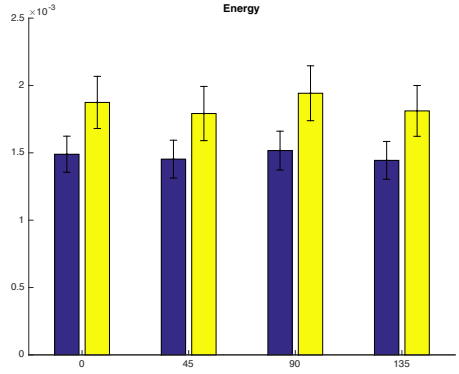

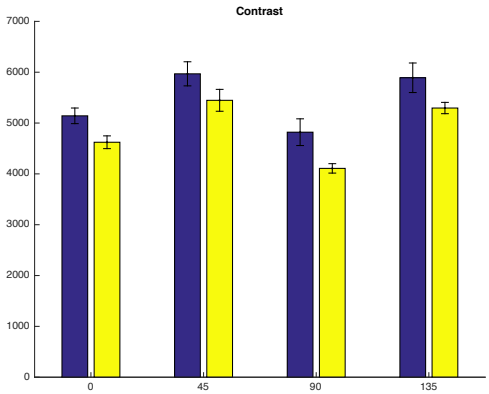

1.5um 500mil/mL vs gelatin SGLDM Bar graphs

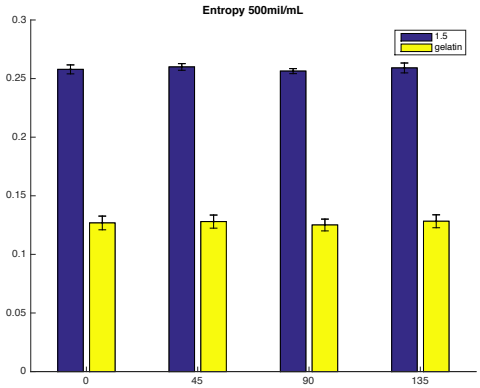

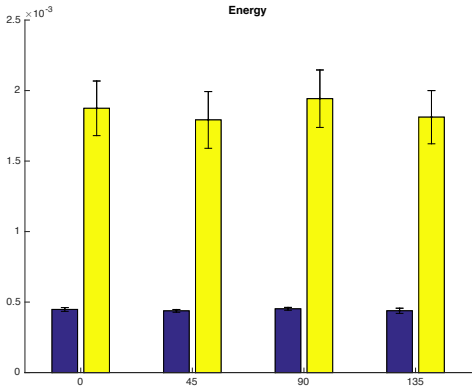

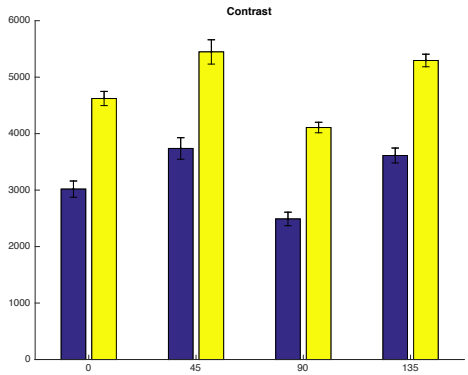

1.5um 100mil/mL vs gelatin processed images SGLDM Bar graphs

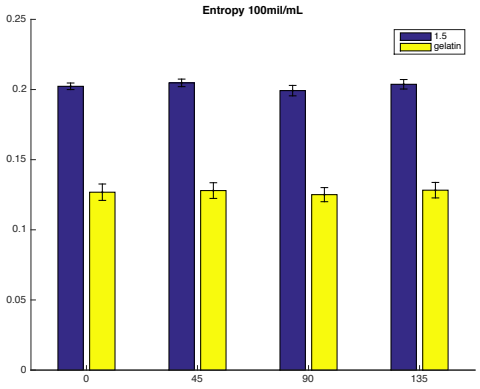

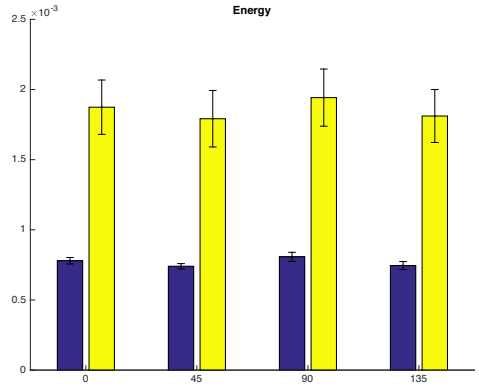

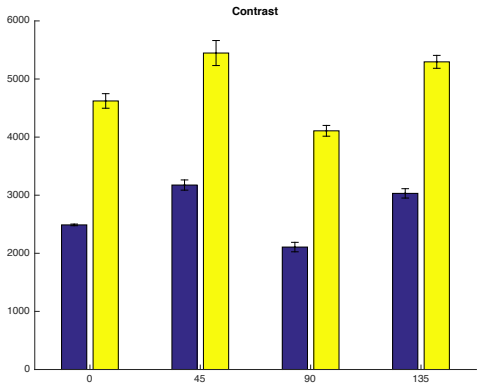

1.5um 25mil/mL vs gelatin processed images SGLDM Bar graphs

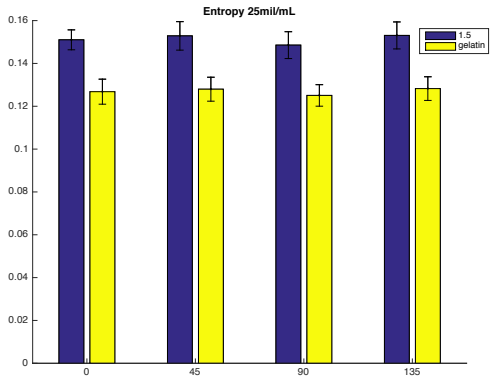

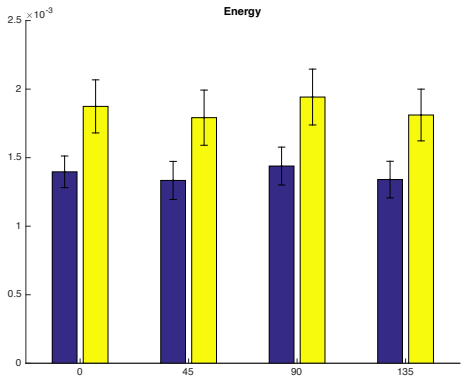

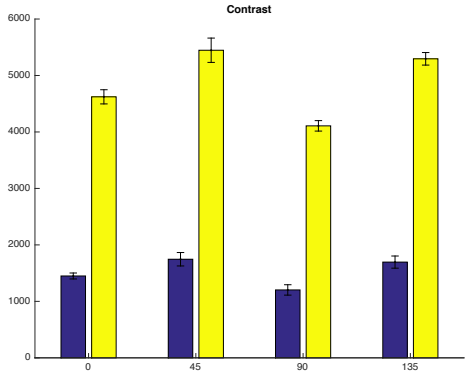

1.5um 2.5mil/mL vs gelatin processed images SGLDM Bar graphs

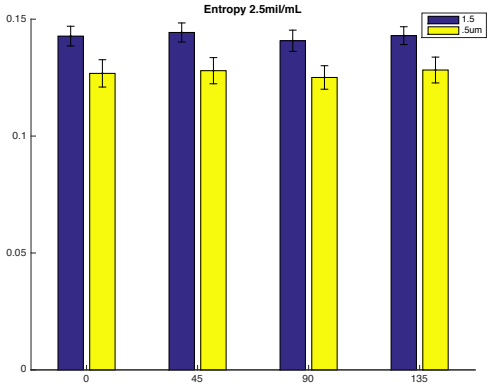

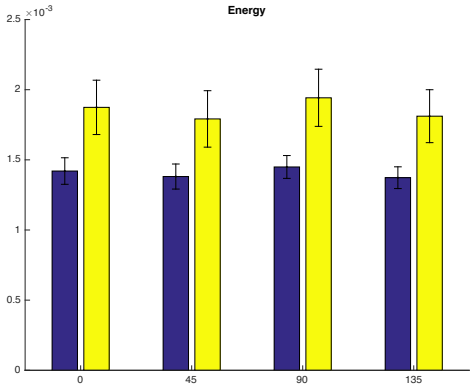

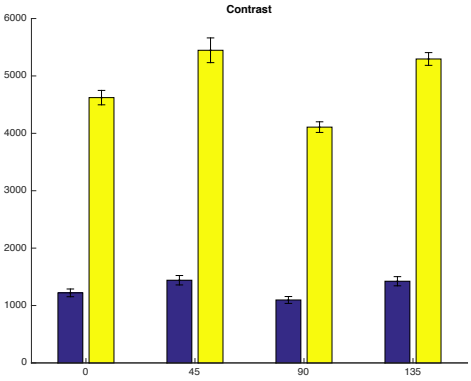

1.5um vs .5um 500mil/mL processed images SGLDM Bar graphs

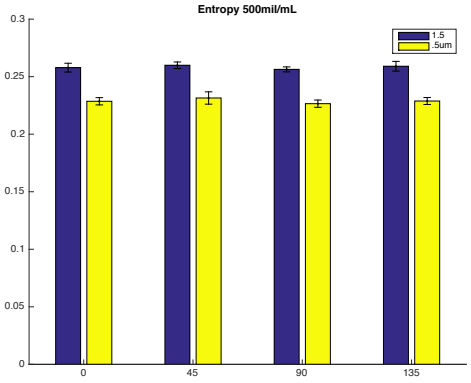

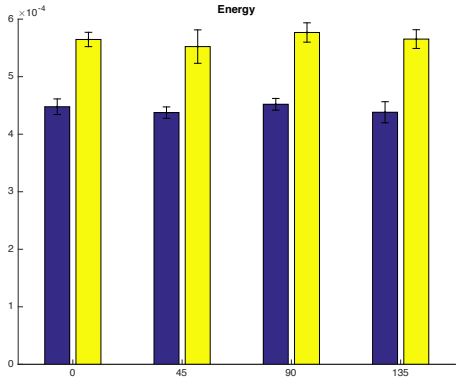

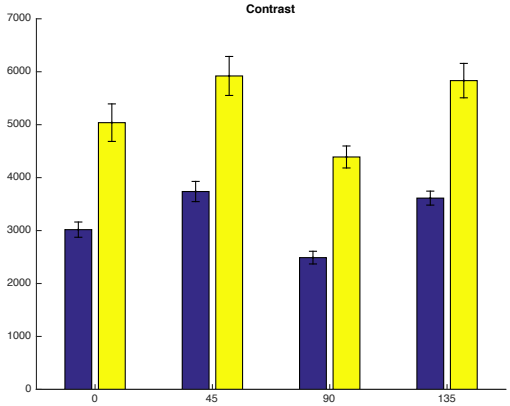

1.5um vs .5um 100mil/mL processed images SGLDM Bar graphs

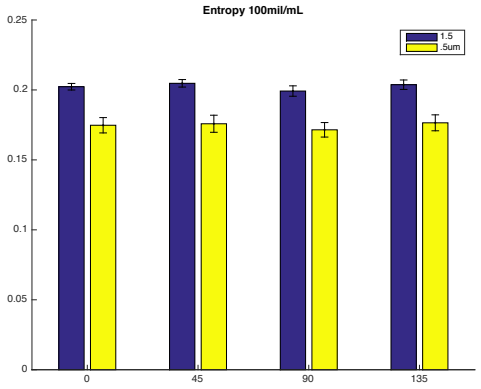

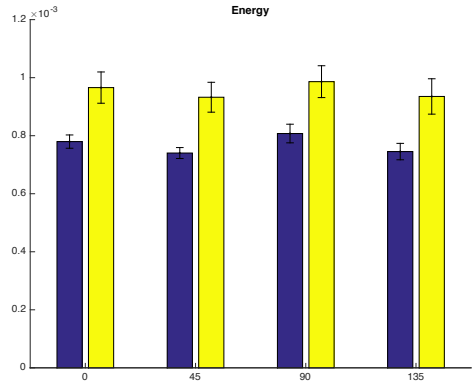

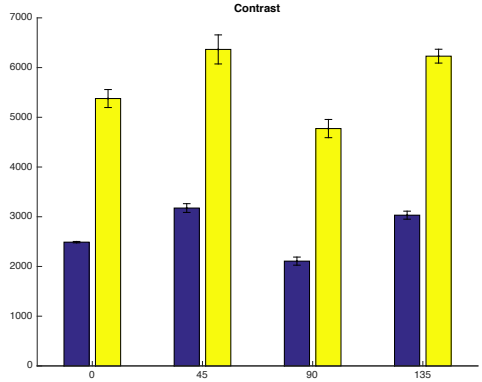

1.5um vs .5um 25mil/mL processed images SGLDM Bar graphs

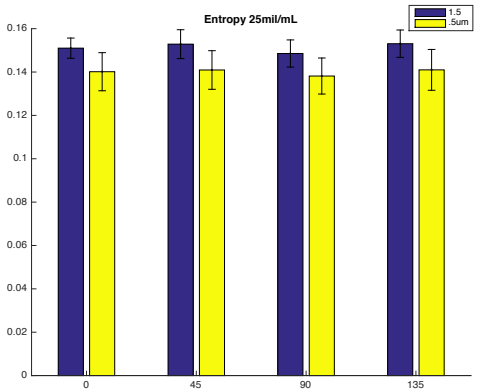

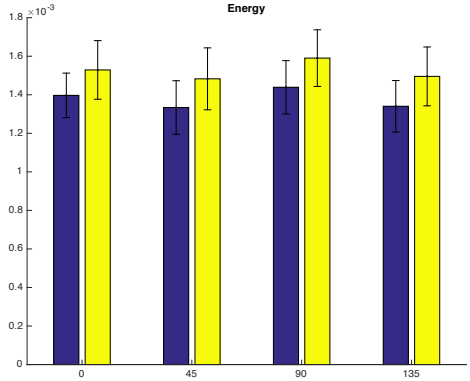

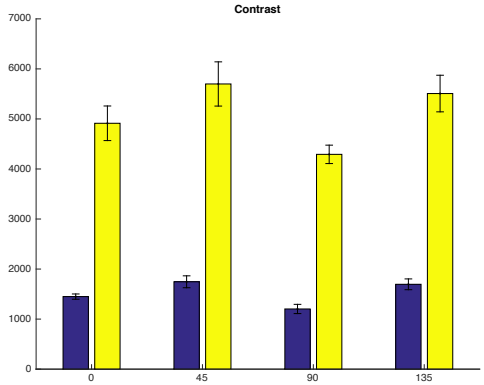

1.5um vs .5um 2.5mil/mL processed images SGLDM Bar graphs

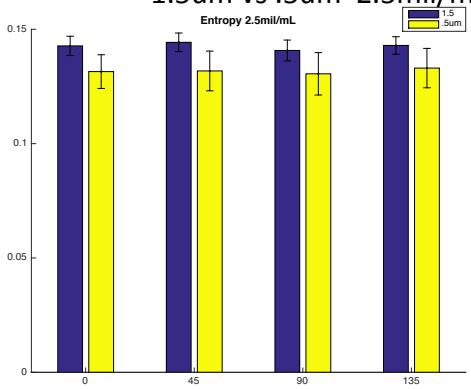

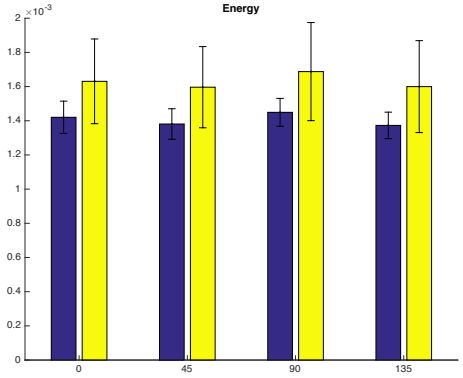

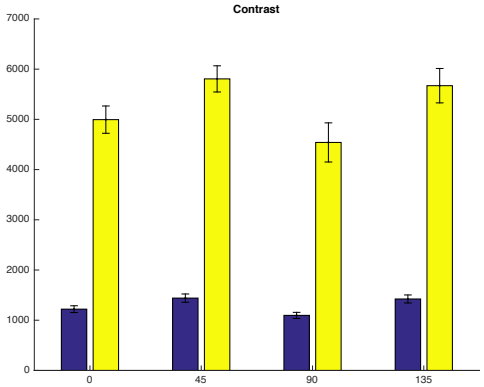

Table 2. Classification results (% correct) for binary gelatin/microsphere gel comparisons. The column headings denote the type of classification scheme used. 7-1, 7-2 and 7-3: all possible combinations of 1, 2, or 3 of the top seven features, respectively. 7-ALL: all possible combinations of any number of the top seven features. 24–3: all possible combinations of 3 of all 24 features.

Comparison	7-1	7-2	7-3	7-ALL	24-3
			Plain versus 0.49		
2.5 million/ml	61.3	65.1	67.3	66.3	65.1
25 million/ml	63.2	64.7	66.3	66.5	58.3
100 million/ml	96.3	96.1	95.8	96.0	96.8
500 million/ml	95.1	95.1	95.0	94.1	96.1
			Plain versus 1.59		
2.5 million/ml	64.2	68.2	69.6	69.0	70.3
25 million/ml	64.6	67.6	68.7	70.8	74.8
100 million/ml	81.6	85.3	86.3	85.5	84.8
500 million/ml	96.6	97.5	98.1	98.8	98.6
			Plain versus 3.01		
2.5 million/ml	71.6	71.3	70.0	70.0	73.1
25 million/ml	80.2	80.5	78.7	81.3	83.7
100 million/ml	81.8	87.3	87.3	89.1	85.3
500 million/ml	99.6	99.5	99.3	99.3	100.0
			0.49 versus 1.59		
2.5 million/ml	59.6	66.3	66.6	66.7	71.2
25 million/ml	69.6	73.8	72.8	72.8	79.4
100 million/ml	89.1	89.1	89.2	90.0	90.6
500 million/ml	91.0	92.0	94.1	94.1	92.0
			0.49 versus 3.01		
2.5 million/ml	78.0	77.0	77.6	78.0	76.3
25 million/ml	82.3	83.7	85.6	82.6	86.2
100 million/ml	92.1	94.3	95.8	95.6	98.6
500 million/ml	96.	96.6	97.5	98.6	100.0
			1.59 versus 3.01		
2.5 million/ml	67.3	68.0	65.3	67.8	70.7
25 million/ml	63.1	65.7	65.1	67.6	66.3
100 million/ml	75.0	74.5	70.7	72.5	75.3
500 million/ml	76.1	85.0	83.5	86.0	95.5

Figure 40 Results report from Gossage et al. [15]

Appendix 4 MATLAB Code

MATLAB CODE FOR DFT ANALYSIS

```
x2=imread('/Users/Bandukwala/Documents/MATLAB/OCT images/dr tearney
images/wire_crop_10_6.jpg');
x=x2(:,:,1);
xfft=abs(fft2(x));
xshift=fftshift(xfft);
n=length(xshift);
fq=floor(n/8);
sq=floor(n/4);
tq=floor(3*n/8);
foq=n/2;
xshift_fq=xshift((n/2-fq):(n/2+fq),(n/2-fq):(n/2+fq));
xshift_sq=xshift((n/2-sq):(n/2+sq),(n/2-sq):(n/2+sq));

for i=floor(length(xshift_sq)/2)-fq:floor(length(xshift_sq)/2)+fq
    for j=floor(length(xshift_sq)/2)-fq:floor(length(xshift_sq)/2)+fq
     xshift_sq(i,j)=0;
    end
end

xshift_tq=xshift((n/2-tq):(n/2+tq),(n/2-tq):(n/2+tq));

for i=floor(length(xshift_tq)/2)-sq:floor(length(xshift_tq)/2)+sq
    for j=floor(length(xshift_tq)/2)-sq:floor(length(xshift_tq)/2)+sq
     xshift_tq(i,j)=0;
    end
end

xshift_foq=xshift;

for i=floor(length(xshift_foq)/2)-tq:floor(length(xshift_foq)/2)+tq
    for j=floor(length(xshift_foq)/2)-tq:floor(length(xshift_foq)/2)+tq
     xshift_foq(i,j)=0;
    end
end

intfq=trapz(trapz(xshift_fq))
intsq=trapz(trapz(xshift_sq))
inttq=trapz(trapz(xshift_tq))
intfoq=trapz(trapz(xshift_foq))

total_magnitude=intfq+intsq+inttq+intfoq

percent_fq=intfq/total_magnitude;
percent_sq=intsq/total_magnitude;
percent_tq=inttq/total_magnitude;
percent_foq=intfoq/total_magnitude;

figure()
hold on
imagesc(xshift)
colorbar
```

```
caxis([0 10000])
colormap(gray)
title('BE Phantom')
hold off


x15=imread('/Users/Bandukwala/Documents/MATLAB/OCT
images/evaluation/esophagus_hsing_fda.png');
x15=x15(:,:,1);
xfft15=abs(fft2(x15));
xshift15=fftshift(xfft15);
n15=length(xshift15);
fq15=floor(n15/8);
sq15=floor(n15/4);
tq15=floor(3*n15/8);
foq15=n15/2;
xshift_fq15=xshift15((n15/2-fq15):(n15/2+fq15),(n15/2-
fq15):(n15/2+fq15));
xshift_sq15=xshift15((n15/2-sq15):(n15/2+sq15),(n15/2-
sq15):(n15/2+sq15));

for i=floor(length(xshift_sq15)/2)-
fq15:floor(length(xshift_sq15)/2)+fq15
    for j=floor(length(xshift_sq15)/2)-
fq15:floor(length(xshift_sq15)/2)+fq15
     xshift_sq15(i,j)=0;
    end
end

xshift_tq15=xshift15((n15/2-tq15):(n15/2+tq15),(n15/2-
tq15):(n15/2+tq15));

for i=floor(length(xshift_tq15)/2)-
sq15:floor(length(xshift_tq15)/2)+sq15
    for j=floor(length(xshift_tq15)/2)-
sq15:floor(length(xshift_tq15)/2)+sq15
     xshift_tq15(i,j)=0;
    end
end

xshift_foq15=xshift15;

for i=floor(length(xshift_foq15)/2)-
tq15:floor(length(xshift_foq15)/2)+tq15
    for j=floor(length(xshift_foq15)/2)-
tq15:floor(length(xshift_foq15)/2)+tq15
     xshift_foq15(i,j)=0;
    end
end

intfq15=trapz(trapz(xshift_fq15))
intsq15=trapz(trapz(xshift_sq15))
inttq15=trapz(trapz(xshift_tq15))
intfoq15=trapz(trapz(xshift_foq15))

total_magnitude15=intfq15+intsq15+inttq15+intfoq15
```

```
percent_fq15=intfq15/total_magnitude15;
percent_sq15=intsq15/total_magnitude15;
percent_tq15=inttq15/total_magnitude15;
percent_foq15=intfoq15/total_magnitude15;

figure()
hold on
imagesc(xshift15)
colorbar
caxis([0 10000])
colormap(gray)
title('Normal Esophagus Phantom')
hold off

x500=imread('/Users/Bandukwala/Documents/MATLAB/OCT images/dr tearney
images/slide43_118_3.jpg');
%x500=imcomplement(x500);
x500=x500(:,:,1);
xfft500=abs(fft2(x500));
xshift500=fftshift(xfft500);
n500=length(xshift500);
fq500=floor(n500/8);
sq500=floor(n500/4);
tq500=floor(3*n500/8);
foq500=n500/2;
xshift_fq500=xshift500((n500/2-fq500):(n500/2+fq500),(n500/2-
fq500):(n500/2+fq500));
xshift_sq500=xshift500((n500/2-sq500):(n500/2+sq500),(n500/2-
sq500):(n500/2+sq500));

for i=floor(length(xshift_sq500)/2)-
fq500:floor(length(xshift_sq500)/2)+fq500
    for j=floor(length(xshift_sq500)/2)-
fq500:floor(length(xshift_sq500)/2)+fq500
     xshift_sq500(i,j)=0;
    end
end

xshift_tq500=xshift500((n500/2-tq500):(n500/2+tq500),(n500/2-
tq500):(n500/2+tq500));

for i=floor(length(xshift_tq500)/2)-
sq500:floor(length(xshift_tq500)/2)+sq500
    for j=floor(length(xshift_tq500)/2)-
sq500:floor(length(xshift_tq500)/2)+sq500
     xshift_tq500(i,j)=0;
    end
end

xshift_foq500=xshift500;

for i=floor(length(xshift_foq500)/2)-
tq500:floor(length(xshift_foq500)/2)+tq500
    for j=floor(length(xshift_foq500)/2)-
tq500:floor(length(xshift_foq500)/2)+tq500
     xshift_foq500(i,j)=0;
```

```
    end
end

intfq500=trapz(trapz(xshift_fq500))
intsq500=trapz(trapz(xshift_sq500))
inttq500=trapz(trapz(xshift_tq500))
intfoq500=trapz(trapz(xshift_foq500))

total_magnitude500=intfq500+intsq500+inttq500+intfoq500

percent_fq500=intfq500/total_magnitude500;
percent_sq500=intsq500/total_magnitude500;
percent_tq500=inttq500/total_magnitude500;
percent_foq500=intfoq500/total_magnitude500;

figure()
hold on
imagesc(xshift500)
colorbar
caxis([0 10000])
colormap(gray)
title('BE Clinical')
hold off

x00=imread('/Users/Bandukwala/Documents/MATLAB/OCT images/dr tearney
images/slide7sq_118_2.jpg');
%x00=imcomplement(x500);
x00=x00(:,:,1);
xfft00=abs(fft2(x00));
xshift00=fftshift(xfft00);
n00=length(xshift00);
fq00=floor(n00/8);
sq00=floor(n00/4);
tq00=floor(3*n00/8);
foq00=n00/2;
xshift_fq00=xshift00((n00/2-fq00):(n00/2+fq00),(n00/2-
fq00):(n00/2+fq00));
xshift_sq00=xshift00((n00/2-sq00):(n00/2+sq00),(n00/2-
sq00):(n00/2+sq00));

for i=floor(length(xshift_sq00)/2)-
fq00:floor(length(xshift_sq00)/2)+fq00
    for j=floor(length(xshift_sq00)/2)-
fq00:floor(length(xshift_sq00)/2)+fq00
     xshift_sq00(i,j)=0;
    end
end

xshift_tq00=xshift00((n00/2-tq00):(n00/2+tq00),(n00/2-
tq00):(n00/2+tq00));

for i=floor(length(xshift_tq00)/2)-
sq00:floor(length(xshift_tq00)/2)+sq00
    for j=floor(length(xshift_tq00)/2)-
sq00:floor(length(xshift_tq00)/2)+sq00
     xshift_tq00(i,j)=0;
    end
```

```
end

xshift_foq00=xshift00;

for i=floor(length(xshift_foq00)/2)-
tq00:floor(length(xshift_foq00)/2)+tq00
    for j=floor(length(xshift_foq00)/2)-
tq00:floor(length(xshift_foq00)/2)+tq00
     xshift_foq00(i,j)=0;
    end
end

intfq00=trapz(trapz(xshift_fq00))
intsq00=trapz(trapz(xshift_sq00))
inttq00=trapz(trapz(xshift_tq00))
intfoq00=trapz(trapz(xshift_foq00))

total_magnitude00=intfq00+intsq00+inttq00+intfoq00

percent_fq00=intfq00/total_magnitude00;
percent_sq00=intsq00/total_magnitude00;
percent_tq00=inttq00/total_magnitude00;
percent_foq00=intfoq00/total_magnitude00;

figure()
hold on
imagesc(xshift00)
colorbar
caxis([0 10000])
colormap(gray)
title('Normal Esophagus Clinical')
hold off
```

MATLAB CODE SPATIAL GRAY LEVEL DEPENDCIES MATRIX (SGLDM)

```
clc
clear all
x1=imread('/Users/Bandukwala/Documents/MATLAB/OCT images/dr tearney
images/slide6_118.jpg');
x2=imread('/Users/Bandukwala/Documents/MATLAB/OCT images/dr tearney
images/slide9_118.jpg');
x3=imread('/Users/Bandukwala/Documents/MATLAB/OCT images/dr tearney
images/slide11_118.jpg');
x4=imread('/Users/Bandukwala/Documents/MATLAB/OCT images/dr tearney
images/slide14_118.jpg');
x5=imread('/Users/Bandukwala/Documents/MATLAB/OCT images/dr tearney
images/slide18_118_4.jpg');
x6=imread('/Users/Bandukwala/Documents/MATLAB/OCT images/dr tearney
images/slide24_118_2.jpg');
x7=imread('/Users/Bandukwala/Documents/MATLAB/OCT images/dr tearney
images/slide28_118.jpg');
x8=imread('/Users/Bandukwala/Documents/MATLAB/OCT images/dr tearney
images/slide33_118_2.jpg');
x9=imread('/Users/Bandukwala/Documents/MATLAB/OCT images/dr tearney
images/slide35_118.jpg');
x10=imread('/Users/Bandukwala/Documents/MATLAB/OCT images/dr tearney
images/slide39_118.jpg');
x11=imread('/Users/Bandukwala/Documents/MATLAB/OCT images/dr tearney
images/slide43_118_3.jpg');
x12=imread('/Users/Bandukwala/Documents/MATLAB/OCT images/dr tearney
images/slide2sq_118_3.jpg');
x13=imread('/Users/Bandukwala/Documents/MATLAB/OCT images/dr tearney
images/slide7sq_118_2.jpg');
x14=imread('/Users/Bandukwala/Documents/MATLAB/OCT images/dr tearney
images/slide13sq_118.jpg');
x15=imread('/Users/Bandukwala/Documents/MATLAB/OCT images/dr tearney
images/slide19sq_118_2.jpg');
x16=imread('/Users/Bandukwala/Documents/MATLAB/OCT images/dr tearney
images/slide21sq_118_2.jpg');
x17=imread('/Users/Bandukwala/Documents/MATLAB/OCT images/dr tearney
images/wire_crop_10_6.jpg');
x18=imread('/Users/Bandukwala/Documents/MATLAB/OCT
images/evaluation/esophagus_hsing_fda.png');

a=zeros(118,118,1,'uint8');
a(:,:,1)=(x1(:,:,1));
a(:,:,2)=(x2(:,:,1));
a(:,:,3)=(x3(:,:,1));
a(:,:,4)=(x4(:,:,1));
a(:,:,5)=(x5(:,:,1));
a(:,:,6)=(x6(:,:,1));
a(:,:,7)=(x7(:,:,1));
a(:,:,8)=(x8(:,:,1));
a(:,:,9)=(x9(:,:,1));
a(:,:,10)=(x10(:,:,1));
a(:,:,11)=(x11(:,:,1));
a(:,:,12)=(x12(:,:,1));
a(:,:,13)=(x13(:,:,1));
a(:,:,14)=(x14(:,:,1));
a(:,:,15)=(x15(:,:,1));
a(:,:,16)=(x16(:,:,1));
```

```
a(:,:,17)=(x17(:,:,1));
a(:,:,18)=(x18(:,:,1));

for i=1:18
    a1=a(:,:,i);
    e(i)=entropy(a1);
end

offsets = [0 1;-1 1;-1 0;-1 -1];

for i=1:18
a1=a(:,:,i);
GLCMS = graycomatrix(a1,'NumLevel',256,'Offset',offsets);
stats(i) = graycoprops(GLCMS,'Energy Contrast Correlation');
for j=1:4
    g(i,j)=entropy(GLCMS(:,:,j));
end
end

figure(1)
avger(2,:)=mean(g(1:11,:));
errorer(2,:)=std(g(1:11,:));
avger(1,:)=mean(g(12:16,:));
errorer(1,:)=std(g(12:16,:));
avger(3,:)=(g(18,:));
errorer(3,:)=0;
avger(4,:)=(g(17,:));
errorer(4,:)=0;
hold on
hb=bar(1:4,avger');
pause(0.1); %pause allows the figure to be created
figure(1)
for ib = 1:numel(hb)
    %XData property is the tick labels/group centers; XOffset is the
offset
    %of each distinct group
    xData = hb(ib).XData+hb(ib).XOffset;
    errorbar(xData,avger(ib,:),errorer(ib,:),'k.')
end
labels={'0','45','90','135'}
set(gca, 'XTick', 1:4, 'XTickLabels',labels);
title('Entropy')
legend('Normal Esophagus Clinical','BE Clinical','Normal Phantom','BE
Phantom')
hold off

figure(2)
[en(1,:), en(2,:), en(3,:),
en(4,:),en(5,:),en(6,:),en(7,:),en(8,:),en(9,:),en(10,:),en(11,:),en(12
,:),en(13,:),en(14,:),en(15,:),en(16,:),en(17,:),en(18,:)] =
stats.Energy;
avgen(2,:)=mean(en(1:11,:));
erroren(2,:)=std(en(1:11,:));
avgen(1,:)=mean(en(12:16,:));
erroren(1,:)=std(en(12:16,:));
avgen(3,:)=(en(18,:));
erroren(3,:)=0;
```

```
avgen(4,:)=(en(17,:));
erroren(4,:)=0;
hold on
hb1=bar(1:4,avgen');
% For each set of bars, find the centers of the bars, and write error
bars
pause(0.1); %pause allows the figure to be created
figure(2)

for ib1 = 1:numel(hb1)
    %XData property is the tick labels/group centers; XOffset is the
offset
    %of each distinct group
    xData1 = hb1(ib1).XData+hb1(ib1).XOffset;
    errorbar(xData1,avgen(ib1,:),erroren(ib1,:),'k.')
end
labels={'0','45','90','135'};
set(gca, 'XTick', 1:4, 'XTickLabels',labels);
title('Energy')
hold off

figure(3)
[cn(1,:), cn(2,:), cn(3,:), cn(4,:), cn(5,:), cn(6,:), cn(7,:),
cn(8,:), cn(9,:), cn(10,:),
cn(11,:),cn(12,:),cn(13,:),cn(14,:),cn(15,:),cn(16,:),cn(17,:),cn(18,:)
] = stats.Contrast;
avgcn(2,:)=mean(cn(1:11,:));
errorcn(2,:)=std(cn(1:11,:));
avgcn(1,:)=mean(cn(12:16,:));
errorcn(1,:)=std(cn(12:16,:));
avgcn(3,:)=(cn(18,:));
erroercn(3,:)=0;
avgcn(4,:)=(cn(17,:));
errorcn(4,:)=0;
hold on
hb2=bar(1:4,avgcn');
% For each set of bars, find the centers of the bars, and write error
bars

pause(0.1); %pause allows the figure to be created
figure(3)

for ib2 = 1:numel(hb2)
    %XData property is the tick labels/group centers; XOffset is the
offset
    %of each distinct group
    xData2 = hb2(ib2).XData+hb2(ib2).XOffset;
    errorbar(xData2,avgcn(ib2,:),errorcn(ib2,:),'k.')
end
labels={'0','45','90','135'};
set(gca, 'XTick', 1:4, 'XTickLabels',labels);
title('Contrast')

[her,per,cier,statser]=ttest2(g(1:11,:),g(12:16,:))
[hen,pen,cien,statsen]=ttest2(en(1:11,:),en(12:16,:))
[hcn,pcn,cicn,statscn]=ttest2(cn(1:11,:),cn(12:16,:))
```

MATLAB CODE FOR CENTER SYMMETRIC AUTOCORRELATION (CSAC) FUNCTION

```
clear all
clc

xnorm=imread('/Users/Bandukwala/Documents/MATLAB/OCT images/dr tearney
images/slide7sq_118_2.jpg');
xnorm=double(xnorm(:,:,1));

xBE=imread('/Users/Bandukwala/Documents/MATLAB/OCT images/dr tearney
images/slide43_118_3.jpg');
xBE=double(xBE(:,:,1));

xslide6=imread('/Users/Bandukwala/Documents/MATLAB/OCT
images/evaluation/esophagus_hsing_fda.png');
xslide6=double(xslide6(:,:,1));

xslide43=imread('/Users/Bandukwala/Documents/MATLAB/OCT images/dr
tearney images/wire_crop_10_6.jpg');
xslide43=double(xslide43(:,:,1));

for k=2:117
    i=sub2ind(size(xBE),2,k);
    v=sub2ind(size(xBE),117,k);
    d=1;

    for c=i:v
        uBE(d,k-1)=sum([xBE(c-1) xBE(c+1) xBE(c+118) xBE(c-118)
xBE(c+117) xBE(c-117) xBE(c+119) xBE(c-119)])/8;
        bvarBE(d,k-1)=sum([((xBE(c-1) + xBE(c+1))^2)
((xBE(c+118)+xBE(c-118))^2) ((xBE(c+117)+xBE(c-117))^2)
((xBE(c+119)+xBE(c-119))^2)])/16-uBE(d,k-1)^2;
        wvarBE(d,k-1)=sum([(xBE(c-1)-xBE(c+1))^2 (xBE(c-118)-
xBE(c+118))^2 (xBE(c-117)-xBE(c+117))^2 (xBE(c-119)-xBE(c+119))^2])/16;
        scovBE(d,k-1)=sum([((xBE(c-1)-uBE(d,k-1))*(xBE(c+1)-uBE(d,k-
1))) ((xBE(c+118)-uBE(d,k-1))*(xBE(c-118)-uBE(d,k-1))) ((xBE(c+117)-
uBE(d,k-1))*(xBE(c-117)-uBE(d,k-1))) ((xBE(c+119)-uBE(d,k-1))*(xBE(c-
119)-uBE(d,k-1)))])/4;
        varBE(d,k-1)=sum([((xBE(c-1)^2 + xBE(c+1)^2))
((xBE(c+118)^2+xBE(c-118)^2)) ((xBE(c+117)^2+xBE(c-117)^2))
((xBE(c+119)^2+xBE(c-119)^2))])/8-uBE(d,k-1)^2;
        d=d+1;
    end

end
svrBE=wvarBE./bvarBE;
sacBE=scovBE./varBE;

for k=2:117
    i=sub2ind(size(xnorm),2,k);
    v=sub2ind(size(xnorm),117,k);
    d=1;

    for c=i:v
        unorm(d,k-1)=sum([xnorm(c-1) xnorm(c+1) xnorm(c+118) xnorm(c-
118) xnorm(c+117) xnorm(c-117) xnorm(c+119) xnorm(c-119)])/8;
```

```
        bvarnorm(d,k-1)=sum([((xnorm(c-1) + xnorm(c+1))^2)
((xnorm(c+118)+xnorm(c-118))^2) ((xnorm(c+117)+xnorm(c-117))^2)
((xnorm(c+119)+xnorm(c-119))^2)])/16-unorm(d,k-1)^2;
        wvarnorm(d,k-1)=sum([(xnorm(c-1)-xnorm(c+1))^2 (xnorm(c-118)-
xnorm(c+118))^2 (xnorm(c-117)-xnorm(c+117))^2 (xnorm(c-119)-
xnorm(c+119))^2])/16;
        scovnorm(d,k-1)=sum([((xnorm(c-1)-unorm(d,k-1))*(xnorm(c+1)-
unorm(d,k-1))) ((xnorm(c+118)-unorm(d,k-1))*(xnorm(c-118)-unorm(d,k-
1))) ((xnorm(c+117)-unorm(d,k-1))*(xnorm(c-117)-unorm(d,k-1)))
((xnorm(c+119)-unorm(d,k-1))*(xnorm(c-119)-unorm(d,k-1)))])/4;
        varnorm(d,k-1)=sum([((xnorm(c-1)^2 + xnorm(c+1)^2))
((xnorm(c+118)^2+xnorm(c-118)^2)) ((xnorm(c+117)^2+xnorm(c-117)^2))
((xnorm(c+119)^2+xnorm(c-119)^2))])/8-unorm(d,k-1)^2;
        d=d+1;
    end

end
svrnorm=wvarnorm./bvarnorm;
sacnorm=scovnorm./varnorm;

for k=2:117
    i=sub2ind(size(xslide6),2,k);
    v=sub2ind(size(xslide6),117,k);
    d=1;

    for c=i:v
        uslide6(d,k-1)=sum([xslide6(c-1) xslide6(c+1) xslide6(c+118)
xslide6(c-118) xslide6(c+117) xslide6(c-117) xslide6(c+119) xslide6(c-
119)])/8;
        bvarslide6(d,k-1)=sum([((xslide6(c-1) + xslide6(c+1))^2)
((xslide6(c+118)+xslide6(c-118))^2) ((xslide6(c+117)+xslide6(c-117))^2)
((xslide6(c+119)+xslide6(c-119))^2)])/16-uslide6(d,k-1)^2;
        wvarslide6(d,k-1)=sum([(xslide6(c-1)-xslide6(c+1))^2
(xslide6(c-118)-xslide6(c+118))^2 (xslide6(c-117)-xslide6(c+117))^2
(xslide6(c-119)-xslide6(c+119))^2])/16;
        scovslide6(d,k-1)=sum([((xslide6(c-1)-uslide6(d,k-
1))*(xslide6(c+1)-uslide6(d,k-1))) ((xslide6(c+118)-uslide6(d,k-
1))*(xslide6(c-118)-uslide6(d,k-1))) ((xslide6(c+117)-uslide6(d,k-
1))*(xslide6(c-117)-uslide6(d,k-1))) ((xslide6(c+119)-uslide6(d,k-
1))*(xslide6(c-119)-uslide6(d,k-1)))])/4;
        varslide6(d,k-1)=sum([((xslide6(c-1)^2 + xslide6(c+1)^2))
((xslide6(c+118)^2+xslide6(c-118)^2)) ((xslide6(c+117)^2+xslide6(c-
117)^2)) ((xslide6(c+119)^2+xslide6(c-119)^2))])/8-uslide6(d,k-1)^2;
        d=d+1;
    end

end
svrslide6=wvarslide6./bvarslide6;
sacslide6=scovslide6./varslide6;

for k=2:117
    i=sub2ind(size(xslide43),2,k);
    v=sub2ind(size(xslide43),117,k);
    d=1;

    for c=i:v
        uslide43(d,k-1)=sum([xslide43(c-1) xslide43(c+1)
```

```
xslide43(c+118) xslide43(c-118) xslide43(c+117) xslide43(c-117)
xslide43(c+119) xslide43(c-119)])/8;
        bvarslide43(d,k-1)=sum([((xslide43(c-1) + xslide43(c+1))^2)
((xslide43(c+118)+xslide43(c-118))^2) ((xslide43(c+117)+xslide43(c-
117))^2) ((xslide43(c+119)+xslide43(c-119))^2)])/16-uslide43(d,k-1)^2;
        wvarslide43(d,k-1)=sum([(xslide43(c-1)-xslide43(c+1))^2
(xslide43(c-118)-xslide43(c+118))^2 (xslide43(c-117)-xslide43(c+117))^2
(xslide43(c-119)-xslide43(c+119))^2])/16;
        scovslide43(d,k-1)=sum([((xslide43(c-1)-uslide43(d,k-
1))*(xslide43(c+1)-uslide43(d,k-1))) ((xslide43(c+118)-uslide43(d,k-
1))*(xslide43(c-118)-uslide43(d,k-1))) ((xslide43(c+117)-uslide43(d,k-
1))*(xslide43(c-117)-uslide43(d,k-1))) ((xslide43(c+119)-uslide43(d,k-
1))*(xslide43(c-119)-uslide43(d,k-1)))])/4;
        varslide43(d,k-1)=sum([((xslide43(c-1)^2 + xslide43(c+1)^2))
((xslide43(c+118)^2+xslide43(c-118)^2)) ((xslide43(c+117)^2+xslide43(c-
117)^2)) ((xslide43(c+119)^2+xslide43(c-119)^2))])/8-uslide43(d,k-1)^2;

        d=d+1;
    end

end
svrslide43=wvarslide43./bvarslide43;
sacslide43=scovslide43./varslide43;

[yBE,a1]=hist(varBE,100);
[scBE,a2]=hist(scovBE,100);
[wvBE,a3]=hist(wvarBE,100);
[bvBE,a4]=hist(bvarBE,100);
[svBE,a5]=hist(svrBE,100);
[saBE,a6]=hist(sacBE,100);

[ynorm,a7]=hist(varnorm,100);
[scnorm,a8]=hist(scovnorm,100);
[wvnorm,a9]=hist(wvarnorm,100);
[bvnorm,a10]=hist(bvarnorm,100);
[svnorm,a11]=hist(svrnorm,100);
[sanorm,a12]=hist(sacnorm,100);

[yslide6,a13]=hist(varslide6,100);
[scslide6,a14]=hist(scovslide6,100);
[wvslide6,a15]=hist(wvarslide6,100);
[bvslide6,a16]=hist(bvarslide6,100);
[svslide6,a17]=hist(svrslide6,100);
[saslide6,a18]=hist(sacslide6,100);

[yslide43,a19]=hist(varslide43,100);
[scslide43,a20]=hist(scovslide43,100);
[wvslide43,a21]=hist(wvarslide43,100);
[bvslide43,a22]=hist(bvarslide43,100);
[svslide43,a23]=hist(svrslide43,100);
[saslide43,a24]=hist(sacslide43,100);

for z=1:length(a1)
    varBEhist(z)=sum(yBE(z,:));
    scovBEhist(z)=sum(scBE(z,:));
    wvarBEhist(z)=sum(wvBE(z,:));
    bvarBEhist(z)=sum(bvBE(z,:));
```

```
    svrBEhist(z)=sum(svBE(z,:));
    sacBEhist(z)=sum(saBE(z,:));
    varnormhist(z)=sum(ynorm(z,:));
    scovnormhist(z)=sum(scnorm(z,:));
    wvarnormhist(z)=sum(wvnorm(z,:));
    bvarnormhist(z)=sum(bvnorm(z,:));
    svrnormhist(z)=sum(svnorm(z,:));
    sacnormhist(z)=sum(sanorm(z,:));
    varslide6hist(z)=sum(yslide6(z,:));
    scovslide6hist(z)=sum(scslide6(z,:));
    wvarslide6hist(z)=sum(wvslide6(z,:));
    bvarslide6hist(z)=sum(bvslide6(z,:));
    svrslide6hist(z)=sum(svslide6(z,:));
    sacslide6hist(z)=sum(saslide6(z,:));
    varslide43hist(z)=sum(yslide43(z,:));
    scovslide43hist(z)=sum(scslide43(z,:));
    wvarslide43hist(z)=sum(wvslide43(z,:));
    bvarslide43hist(z)=sum(bvslide43(z,:));
    svrslide43hist(z)=sum(svslide43(z,:));
    sacslide43hist(z)=sum(saslide43(z,:));
end
figure()
hold on
plot(a1,varBEhist,a7,varnormhist,a13,varslide6hist,a19,varslide43hist)
title('VAR')
legend('Normal Clinical','BE clinical','Normal Phantom','BE Phantom')
hold off

figure()
hold on
plot(a2,scovBEhist,a8,scovnormhist,a14,scovslide6hist,a20,scovslide43hi
st)
title('SCOV')
legend('Normal Clinical','BE clinical','Normal Phantom','BE Phantom')
hold off

figure()
hold on
plot(a3,wvarBEhist,a9,wvarnormhist,a15,wvarslide6hist,a21,wvarslide43hi
st)
title('WVAR')
legend('Normal Clinical','BE clinical','Normal Phantom','BE Phantom')
hold off

figure()
hold on
plot(a4,bvarBEhist,a10,bvarnormhist,a16,bvarslide6hist,a22,bvarslide43h
ist)
title('BVAR')
legend('Normal Clinical','BE clinical','Normal Phantom','BE Phantom')
hold off

figure()
hold on
plot(a5,svrBEhist,a11,svrnormhist,a17,svrslide6hist,a23,svrslide43hist)
title('SVR')
legend('Normal Clinical','BE clinical','Normal Phantom','BE Phantom')
```

```
hold off

figure()
hold on
plot(a6,sacBEhist,a12,sacnormhist,a18,sacslide6hist,a24,sacslide43hist)
title('SAC')
legend('Normal Clinical','BE clinical','Normal Phantom','BE Phantom')
hold off
```

References:

1. Takubo, K., *Pathology of the Esophagus: An Atlas and Textbook; -With 453 Illustrations, Including 417 in Color*. 2007: Springer.
2. Odze, R.D., *Barrett esophagus: histology and pathology for the clinician.* Nature Reviews Gastroenterology and Hepatology, 2009. **6**(8): p. 478-490.
3. Chen, Y., et al., *Review of advanced imaging techniques.* Journal of pathology informatics, 2012. **3**(1): p. 22.
4. Gora, M.J., et al., *Tethered capsule endomicroscopy enables less invasive imaging of gastrointestinal tract microstructure.* Nature medicine, 2013. **19**(2): p. 238-240.
5. Spechler, S.J., *Barrett esophagus and risk of esophageal cancer: a clinical review.* Jama, 2013. **310**(6): p. 627-636.

6. Vieth, M., et al., *Epithelial Thickness is a Marker of Gastroesophageal Reflux Disease.* Clinical Gastroenterology and Hepatology, 2016. **14**(11): p. 1544-1551. e1.
7. Kenneth K. Wang, M.D.a.R.E.S., M.D., *Updated Guidelines 2008 for the Diagnosis, Surveillance and Therapy of Barrett's Esophagus.* American Journal of Gastroenterology, 2008: p. 10.
8. Association, A.G., *American Gastroenterological Association medical position statement on the management of Barrett's esophagus.* Gastroenterology, 2011. **140**(3): p. 1084-1091.
9. Silverstein, F.E. and G.N. Tytgat, *Atlas of gastrointestinal endoscopy*. 1991.
10. Shaheen, N.J., et al., *ACG clinical guideline: diagnosis and management of Barrett's esophagus.* The American journal of gastroenterology, 2016. **111**(1): p. 30-50.
11. Tsai, T.-H., et al., *Comparison of tissue architectural changes between radiofrequency ablation and cryospray ablation in Barrett's esophagus using endoscopic three-dimensional optical coherence tomography.* Gastroenterology research and practice, 2012. **2012**.
12. Qi, X., et al., *Image analysis for classification of dysplasia in Barrett's esophagus using endoscopic optical coherence tomography.* Biomedical optics express, 2010. **1**(3): p. 825-847.
13. Boas, D.A., C. Pitris, and N. Ramanujam, *Handbook of biomedical optics*. 2011: CRC press.
14. Lamouche, G., et al., *Review of tissue simulating phantoms with controllable optical, mechanical and structural properties for use in optical coherence tomography.* Biomedical optics express, 2012. **3**(6): p. 1381-1398.
15. de Bruin, D.M., et al., *Optical phantoms of varying geometry based on thin building blocks with controlled optical properties.* Journal of biomedical optics, 2010. **15**(2): p. 025001-025001-10.
16. Baxi, J., et al., *Retina-simulating phantom for optical coherence tomography.* Journal of biomedical optics, 2014. **19**(2): p. 021106-021106.
17. Lurie, K.L., et al., *Three-dimensional, distendable bladder phantom for optical coherence tomography and white light cystoscopy.* Journal of biomedical optics, 2014. **19**(3): p. 036009-036009.
18. Harwood, D., et al., *Texture classification by center-symmetric auto-correlation, using Kullback discrimination of distributions.* Pattern Recognition Letters, 1995. **16**(1): p. 1-10.
19. Chen, Y., et al., *Effects of axial resolution improvement on optical coherence tomography (OCT) imaging of gastrointestinal tissues.* Optics express, 2008. **16**(4): p. 2469-2485.
20. Gossage, K.W., et al., *Texture analysis of optical coherence tomography images: feasibility for tissue classification.* Journal of biomedical optics, 2003. **8**(3): p. 570-575.
21. Gossage, K.W., et al., *Texture analysis of speckle in optical coherence tomography images of tissue phantoms.* Physics in medicine and biology, 2006. **51**(6): p. 1563.

22. Schmitt, J.M., S. Xiang, and K.M. Yung, *Speckle in optical coherence tomography.* Journal of biomedical optics, 1999. **4**(1): p. 95-105.
23. Vese, L.A. and S.J. Osher, *Modeling textures with total variation minimization and oscillating patterns in image processing.* Journal of scientific computing, 2003. **19**(1-3): p. 553-572.
24. Shapiro, L.G. and G.C. Stockman, *Computer Vision*. 2001: Prentice Hall.
25. Lee, K.-L. and L.-H. Chen, *A new method for coarse classification of textures and class weight estimation for texture retrieval.* PATTERN RECOGNITION AND IMAGE ANALYSIS C/C OF RASPOZNAVANIYE OBRAZOV I ANALIZ IZOBRAZHENII, 2002. **12**(4): p. 400-410.
26. Poneros, J.M., et al., *Diagnosis of specialized intestinal metaplasia by optical coherence tomography.* Gastroenterology, 2001. **120**(1): p. 7-12.
27. Sauk, J., et al., *Interobserver agreement for the detection of Barrett's esophagus with optical frequency domain imaging.* Digestive diseases and sciences, 2013. **58**(8): p. 2261-2265.
28. Aguirre, A.D., et al., *Cellular resolution ex vivo imaging of gastrointestinal tissues with optical coherence microscopy.* Journal of biomedical optics, 2010. **15**(1): p. 016025-016025-9.
29. Woolsey, N., et al. *Quantitative analysis of low contrast detectability in optical coherence tomography*. in *SPIE Sensing Technology+ Applications*. 2014. International Society for Optics and Photonics.
30. Smith, G.T., et al., *Multimodal 3D cancer-mimicking optical phantom.* Biomedical optics express, 2016. **7**(2): p. 648-662.
31. DeVore, J.R., *Refractive indices of rutile and sphalerite.* JOSA, 1951. **41**(6): p. 416-419.